

This is a non-peer-reviewed preprint submitted to EarthArXiv.

This manuscript has been submitted for publication in *Environmental Science & Technology*. Please note the manuscript has yet to be formally accepted for publication. Subsequent versions of this manuscript may have slightly different content. If accepted, the final version of this manuscript will be available via the 'Peer-Reviewed Publication DOI' link on the right-hand side of this webpage. Please feel free to contact the corresponding authors; we welcome feedback.

1	Aerial LiDAR-Based, Source-Resolved Methane Emissions Inventory: Permian
2	Basin Case Study for Benchmarking U.S. Emissions
3	
4 5 6	Christopher P. Donahue*, Kabir Oberoi, James W. Dillon, Vickira Hengst, Brandon Kennedy, William Kearney, Jackson Lennox, Elizabeth Rehbein, Rory Sykes, Cameron D. Dudiak, Dominic T. Altamura, Gabriel Doherty, Peter A. Roos, Jason K. Brasseur, and Michael J. Thorpe*
7	Bridger Photonics, Inc., Bozeman, MT 59715, USA
8	*Corresponding Authors
9	Email: Christopher.Donahue@bridgerphotonics.com and Mike.Thorpe@bridgerphotonics.com
10	Abstract
11	Reducing methane emissions is one of the quickest ways to slow near-term warming, yet
12	building accurate inventories to track progress towards reduction targets remains challenging.
13	We present a 2024 source-resolved methane inventory for the Permian Basin built from
14	quarterly aerial LiDAR scans that supports benchmarking and provides a scalable framework for
15	operator-level OGMP 2.0 reporting. We combined public infrastructure records with machine
16	learning identification of non-producing sites to define the facility population and generate
17	representative sampling plans, then deployed Bridger Photonics' Gas Mapping LiDAR to scan
18	51,770 sites across four quarters. Sources were localized to within 2 m and attributed to
19	equipment identified in aerial photography acquired during the scans. The instruments

20

21

22

23

24

25

26 27

28

29

30 31

32

33

34

Keywords

- 36 Measurement-based methane inventory, methane intensity, Gas Mapping LiDAR, Aerial LiDAR, OGMP
- 37 2.0 reporting

35

38

42

Synopsis

- 39 We construct a 2024 methane emissions inventory for the Permian Basin using aerial LiDAR, resolving
- 40 emissions to specific equipment and facilities. The results identify major leak sources, enable targeted
- 41 repairs, and establishes a benchmark for setting and tracking emissions reduction targets.

1 Introduction

- 43 Methane's 20-year global warming potential is 80 times that of CO₂, and major anthropogenic
- 44 sources include agriculture, oil and gas, and waste. 1 Cutting methane emissions is widely
- 45 recognized as one of the fastest and most cost-effective strategies to slow near-term climate
- change. In the oil and gas sector, operators have spent the past decade implementing large-
- 47 scale leak detection and repair (LDAR) programs supported by advances in emissions monitoring
- 48 technologies.³ These programs have delivered measurable reductions in some regions, but
- 49 methane emissions remain a major source of uncertainty in greenhouse gas inventories, limiting
- 50 the ability to quantitatively assess mitigation effectiveness and track progress toward reduction
- 51 goals.⁴

52

53

54 55

56

57

58

59 60

61 62

63

64

65

66 67

68

69

Accurate source-resolved methane emissions inventories are essential to inform mitigation strategies, track progress and guide effective policies. Traditional inventories built from activity data and emission factors based on engineering calculations often underestimate emissions. New measurement technologies provide more reliable estimates, enabling inventories at regional, basin, and operator scales. Recognizing this, the United Nations Environment Programme launched the Oil and Gas Methane Partnership (OGMP) 2.0, a global reporting framework designed to improve transparency and scientific credibility. The framework requires companies to transition from conventional factor-based reporting to measurement-informed or measurement-based inventories. More than 150 companies with assets in over 90 countries, representing over 40 percent of global oil and gas production, have joined OGMP 2.0.6 Adoption has grown rapidly, making it a central pathway for industry-wide methane reductions.

Despite rapid advances in methane monitoring, converting observations into accurate operator- or basin-scale inventories remains challenging. In principle, a comprehensive inventory would deliver 1) near-complete spatial coverage with equipment-level resolution, 2) sufficient temporal coverage to capture variability and mitigation, and 3) sufficiently low detection limits with reliable quantification to observe the full emission distribution. In practice, programs balance these elements across technologies and deployment strategies.

Ground-based methods, including handheld instruments, optical gas imaging, and fixed continuous monitors, can excel at source-level diagnosis but do not scale well. For example, handheld OGI campaigns provide detailed attribution yet struggle with accurate emission rate quantification and cannot visit enough facilities frequently enough for regional assessments. Continuous monitors improve temporal coverage but are deployed at relatively few sites, limiting spatial representativeness. Even so, inventories have been built from ground measurements. For example, Omara et al. compiled a 2021 U.S. inventory using measurements from 1,540 facilities collected over several years and extrapolated nationally with infrastructure data. The result is spatially explicit at the facility and regional scale, but sparse temporal sampling reduces sensitivity to short-term mitigation, and the measured facilities may not fully represent all basins and operators.

Spaceborne remote sensing expands spatial reach and temporal sampling but typically has coarser resolution and high detection thresholds, missing many routine sources and complicating attribution. Aerial approaches sit between these extremes because they can cover large producing regions while retaining site- and in some cases source-specific detection and quantification, depending on the technology. Recent studies have leveraged aerial data to construct measurement-based inventories (e.g., Johnson et al.⁸; Sherwin et al.⁹), but accuracy depends on sensor performance and sampling design. For instance, Sherwin et al.⁹ used a basin-scale solar-infrared spectrometer in the Permian that scanned a large share of basin production, but, due to a relatively high detection threshold, captured only a fraction of total emissions and relied on emissions modeling for inventory estimates.

In contrast, Bridger Photonics' Gas Mapping LiDAR (GML) routinely detects sources near 1 kg/h at 90% probability of detection and has supported comprehensive inventories in Canadian provinces,^{8,10} Haynesville Basin (GTI Energy), and in basins throughout Colorado.¹¹ While no technology alone satisfies all ideal criteria, aerial surveys that provide broad spatial coverage, source-level attribution, and sufficiently low detection limits provide a practical solution to enable statistically representative sampling and robust, scalable inventory models.

We present a 2024, measurement-based methane emissions inventory for the Permian Basin derived from a large-scale aerial campaign using Bridger Photonics' GML. This study details the full methodology and assumptions for transparency, while advancing measurement-based inventory practice in three ways:

- We design and execute a representative sampling strategy that combines public
 infrastructure records, machine-learning analysis of recent high-altitude imagery to
 identify non-producing sites missing from public databases, and historical emissions
 information to select basin-representative sites for quarterly scanning.
- 2. We provide the most detailed performance characterization of aerial scans to date, deriving scan-specific site detection sensitivity thresholds and plume-level quantification error estimates based on measurable scan parameters.

- 3. We merge source-level and site-level statistics to propagate uncertainty and scale emissions from the scanned subset to the full basin, explicitly accounting for site emission characteristics and the distribution of equipment counts across facility types.
- The framework is transferable across U.S. basins and enables measurement-based inventories that benchmark methane performance and track progress toward reduction targets.

2 Methods

2.1 Methane Emissions Measurement Data

- This study uses aerial methane emissions data collected with Bridger Photonics' Gas Mapping LiDAR 2.0, hereafter referred to as GML. GML is a remote sensing instrument mounted on manned aircraft that collects topographic and methane concentration point cloud data using two co-aligned scanning lasers, along with coincident aerial photography. GML detects methane emissions at the source level with a localization accuracy of within 2 meters ¹², allowing for attribution to specific equipment or infrastructure at a facility using the aerial imagery that include compressors, flares, generators, facility piping, tanks, separators, vapor recovery units, and wells. Emission rates for detected sources are computed from plume concentration measurements and wind speed data using the method described in Thorpe and Kreitinger.¹³ Facility-level emissions are then estimated by aggregating all source-level emission rates within the facility boundary.
- The performance of GML has been extensively characterized through controlled release studies ^{14–16}, providing one of the most comprehensive performance assessments of any methane detection technology to date. This work has produced a source-level quantification error model ¹⁷ and a probability of detection (PoD) model ¹⁸, both of which are integrated into the total emissions inventory model (described in Section 2.3). The quantification model shows an average single-pass uncertainty of 30% (50% CI) with a positive bias at smaller emission rates (<10 kg/h) and negligible bias at larger emission rates (>10 kg/h). The PoD model describes the likelihood of detecting an emission at a specified rate based on two measured parameters, gas concentration noise (GCN) and wind speed, which collectively capture the influence of deployment parameters and environmental conditions. Under the deployment conditions for this campaign, the average emission rate corresponding to a 90% PoD for all scanned facilities in the campaign was 1.16 kg/h (Supplementary Figure 3).

2.2 Campaign Planning

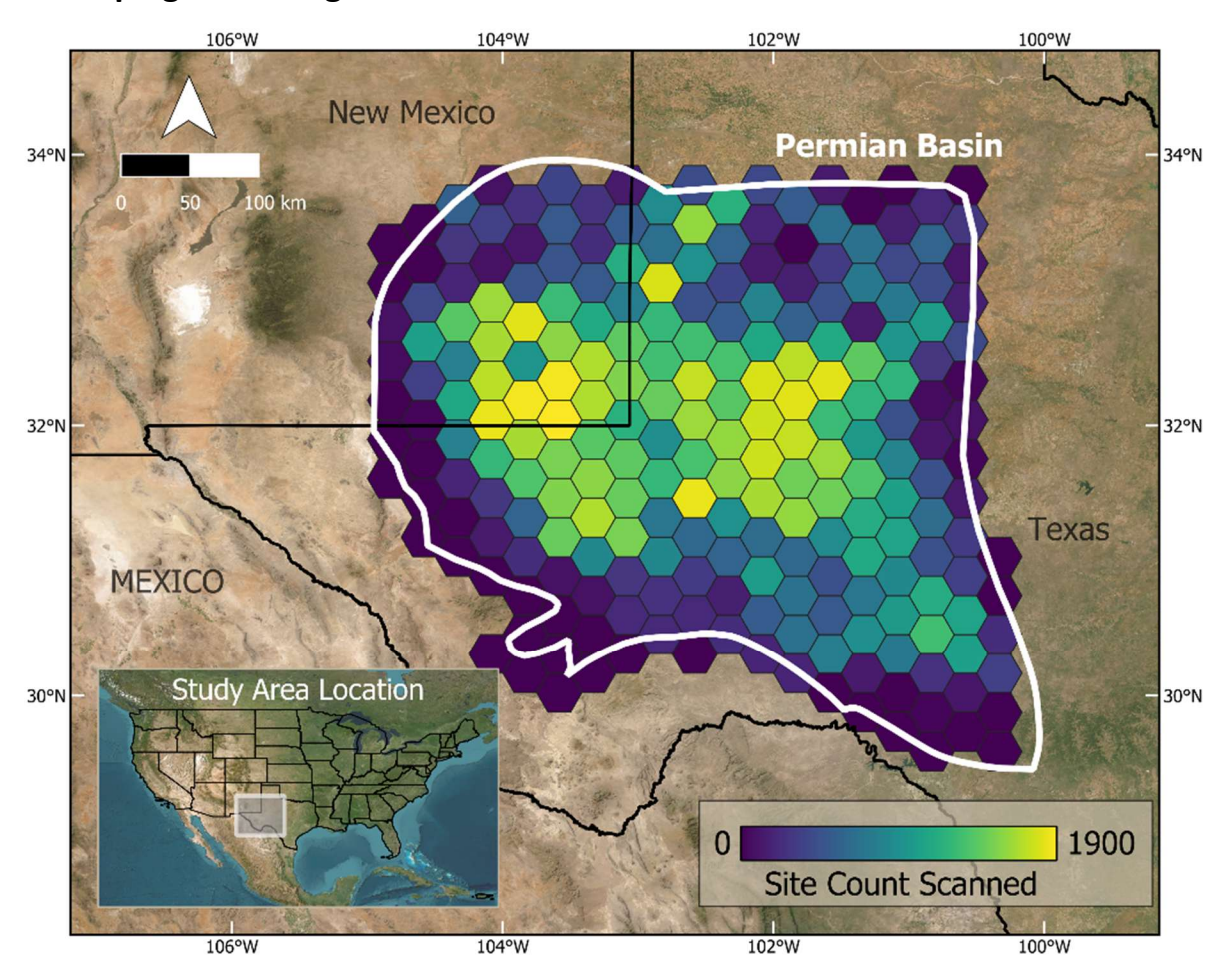


Figure 1. Site sampling heatmap across the Permian Basin campaign, including all four quarters. The Permian Basin boundary is outlined in white, with state borders shown in black. Higher site counts correlate to regions with denser oil and gas activity.

The 2024 aerial measurement campaign in the Permian Basin was designed to scan a representative sample of facilities once per quarter from Q1 through Q4. We first defined the total facility population and its classification, then drew quarterly samples to scan. Facilities were stratified by infrastructure type and production status. Midstream facilities comprised gas processing plants and a combined compressor stations category that groups gathering and transmission compressor stations and gas storage facilities due to similar emission profiles and smaller population sizes. Upstream facilities included wellsites and non-producing sites, which are sites without active wells or reported production that still contain surface infrastructure such as centralized tank batteries. Wellsites were further subdivided by production, measured in barrels of oil equivalent per day (boed): high (>300 boed), standard (15–300 boed), and marginal (<15 boed). These strata were chosen because facility gas production is inversely correlated with methane loss rate ¹⁹, they capture distinct emission profiles, and they align with facility class populations available in state infrastructure databases, which support basin-wide

extrapolation. Gathering pipelines were not targeted during the campaign but were accounted for in the inventory using other aerial measurements (section 2.4).

To determine the population in each stratum, we combined multiple data sources. The Rextag energy infrastructure database provided upstream and midstream assets. Individual wells flagged as active and producing were clustered into facilities using a density-based spatial clustering algorithm.²⁰ Midstream facilities listed in Rextag with an active operational status were incorporated directly into the population count.

Because infrastructure databases do not include non-producing sites (e.g., centralized tank batteries), we developed a machine learning (ML) workflow to identify facility pads and delineate site polygons across the basin from National Agriculture Imagery Program (NAIP) imagery (2022, 0.6 m resolution). The model was most reliable on bare or lightly vegetated pads with clear disturbed earth. Residual false positives arose from visually similar features such as gravel lots, construction pads, and agricultural yards, while false negatives were linked to small or partially vegetated pads and sites with buildings. To estimate the basin-wide count of nonproducing facilities, ML-derived polygons were cross-referenced with the Rextag-identified upstream and midstream sites to remove known locations, leaving a set of supposed nonproducing sites. We then conducted manual quality control over nine geographically distributed areas (covering 7% of the basin area), filtering residual false positives and adding missed sites (Supplementary Figure 1). For each area we computed a non-producing site fraction (# of nonproducing sites per # of producing wellsite) and took the average across areas to obtain a basinwide estimate of 19.2%. Multiplying by the total number of active producing wellsites produced an estimated 21,613 non-producing sites across the basin. Additional methodological details are provided in the SI.

With the population and spatial distribution defined, we drew representative samples during each quarter that measurements were performed. Many gas processing plants and compressor stations were included across all quarters given their relatively small populations and material emissions contribution. The remaining sites were selected via spatially randomized sampling within strata. Sample allocation methods evolved over the campaign as we incorporated learning from earlier quarters; in later quarters we adopted Neyman allocation as the preferred approach (see Supplementary Information, Section S1.3), which was implemented to reduce uncertainty in total emissions estimates. The population and the quarterly sample of sites per stratum is shown in Table 1.

Table 1. Quarterly counts of facilities scanned in 2024 across the Permian Basin by facility stratum. Total Scanned is the sum of Q1-Q4 scan-visits (not necessarily unique facilities). Permian Population is the estimated number of facilities per stratum. Sampling Fraction = Total Scanned \div Permian Population (values > 1 indicate multiple passes per facility).

Facility Stratum	Q1 2024	Q2 2024	Q3 2024	Q4 2024	Total Scanned	Permian Population	Sampling Fraction
Gas Processing Plant	30	29	29	153	241	242	1.00
Compressor Station	333	331	320	635	1,619	939	1.72
Non-Producing	2,465	2,294	2,276	1,437	8,472	21,613	0.39
Wellsite - High	1,867	2,031	2,031	1,437	7,366	6,809	1.08
Wellsite - Standard	2,529	2,644	2,697	2,167	10,037	22,201	0.45
Wellsite - Marginal	6,357	5,848	6,011	5,819	24,035	83,556	0.29
Total Facilities	13,581	13,177	13,364	11,648	51,770	135,360	0.38

Following each quarterly campaign, GML aerial imagery was analyzed to refine facility boundaries and identify all major equipment present. These updated data were used to finalize site stratification. Over the course of the campaign, a total of 51,770 sites were scanned, averaging 12,943 sites per quarter, across 195 calendar days. The campaign sampled sites across all basin areas, providing representative coverage as shown in Figure 1.

2.3 Total Emissions Estimate Method

The total emissions estimation method uses processed GML data as input, organized into quarterly segments. The input data contains key parameters including the facility identifier, aerial scan timestamp, gas detection status (detect or non-detect), emission rate, and equipment type. Additional measurable parameters required for emission modeling include gas concentration noise (GCN), a LiDAR noise metric that condenses the many factors affecting detection sensitivity into a single parameter that represents the noise for each pixel of GML methane concentration imagery, and wind speed, both of which are inputs to the probability of detection (PoD) model. The average signal to noise ratio (SNR) of detected plumes, which characterizes the strength of the elevated methane concentration signal for each detected plume, and wind speed are inputs into the quantification error model.

Our methodology for estimating basin-wide or operator-specific methane emissions inventories builds on prior Monte Carlo frameworks using aerial measurements. 8,9,21 The model integrates detailed performance characterizations, accounts for detection probability and quantification error, and uses facility-specific equipment counts to extrapolate emissions from measured subsets to the full basin population. The result is a comprehensive, bias-corrected inventory composed of (1) directly measured emissions, (2) estimated missed emissions within the partial detection region (0.4 to 3 kg/h), and (3) a 95% confidence interval that combines uncertainty from extrapolation, quantification, sampling, and detection sensitivity. We set an emission rate of 0.4 kg/h as the lower bound to ensure reliable extrapolation and to provide a clear transition point for incorporating smaller sources. Figure 2 presents this workflow from inputs through simulation to inventory assembly.

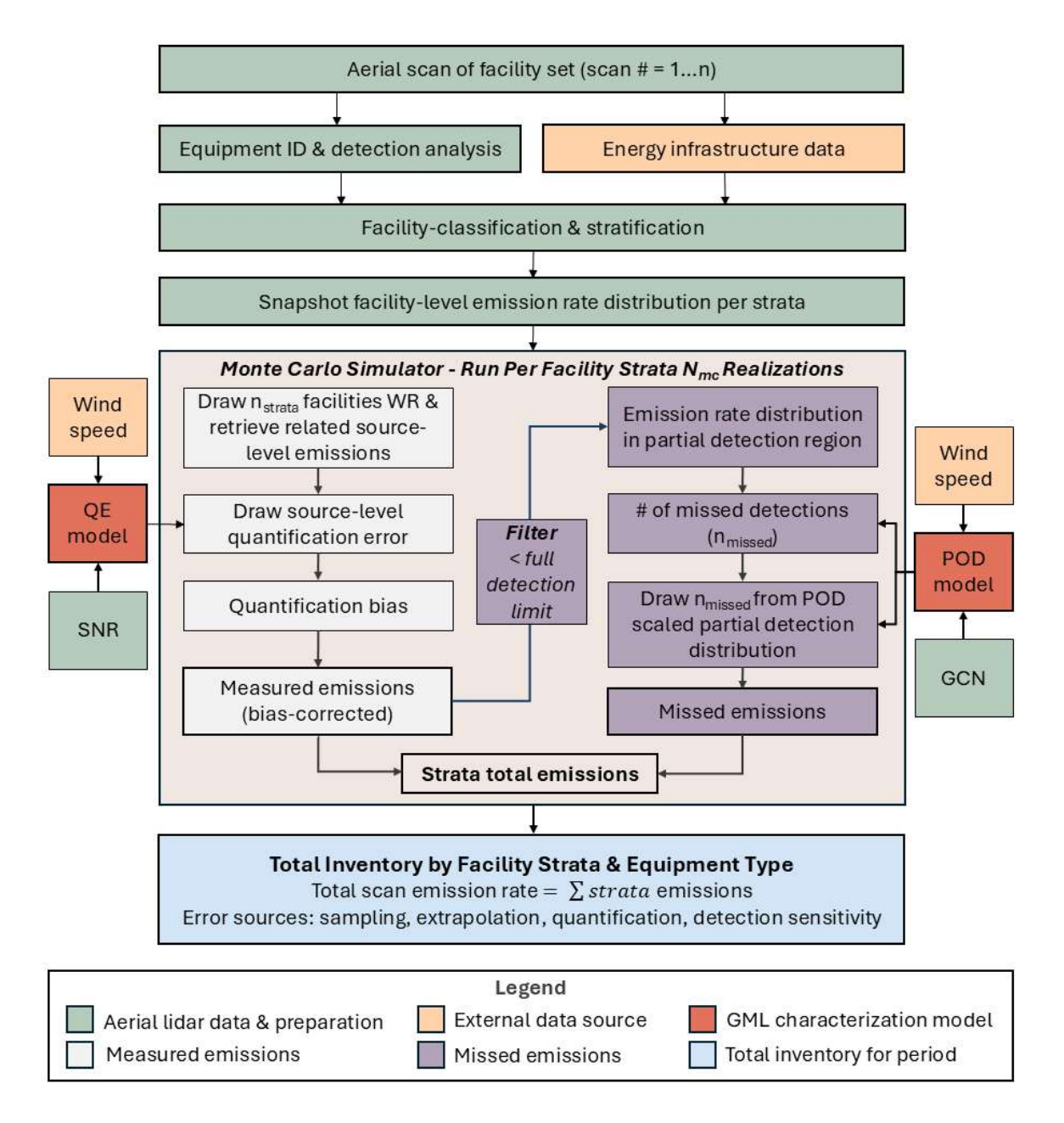


Figure 2. Overview of the workflow for creating a top-down facility-level total emissions inventory with source-resolved aerial flyover data. The inventory framework operates in a hybrid manner, using both facility- and source-level emissions data. Source-resolved emissions are aggregated to the facility-level for spatial and temporal extrapolation, while the source-level emissions are used within the Monte Carlo simulation to account for quantification errors and detection sensitivity.

2.3.1 Emissions Data Pre-Analysis Scheme

Our workflow begins with several pre-analysis steps performed on each quarterly set of facility scan data. Scan data for each site visit was analyzed to identify emitters, estimate fluxes, and map equipment using coincident aerial imagery. We then combine observed equipment counts

and types with external infrastructure and production information from the Rextag database to classify sites and assign each facility to a stratum. This sequence establishes the structured inputs required for inventory construction and for the Monte Carlo simulation that follows.

We next prepare the snapshot emissions rate distribution used in the simulation. For each facility, source level measurements are down selected to a "snapshot" defined as the first observation of each source location during the visit, averaged across detections within a three-hour window to account for overlapping scan swaths and to improve quantification accuracy. If a source is not detected on the first pass but appears on a later pass within that window, it is excluded from the snapshot to avoid inflating event probabilities. This preserves the native frequency of emission events across facilities and equipment types and provides the key input for spatial and temporal extrapolation.

Although GML provides source-level emission measurements, our model operates in a hybrid between facility-level and equipment-level because facility-level counts are the finest resolution available in state infrastructure databases to produce population estimates (i.e., equipment-level populations are not available until a large fraction of the basin has been scanned). Snapshot source-level emissions are aggregated to the facility-level by summing all sources included in the snapshot within the facility boundary. Emission distributions are then produced for each of the six facility strata, which includes facility scans with no detections.

2.3.2 Monte Carlo Framework

Previous studies have used Monte Carlo frameworks that stratify facility-level emissions data and simulate basin-wide emissions by randomly sampling measured facilities within each stratum. ^{8,9} However, we found that even within a single stratum, facility-level emission profiles can vary substantially depending on the specific facilities sampled. By analyzing equipment counts and types identified from GML aerial imagery at each scanned facility, we observed a strong correlation between facility-level emission factors and total equipment counts (Figure 3B). This finding highlights the importance of facility definition and size, particularly equipment count, when extrapolating emissions. Because equipment-count data are largely absent from public energy infrastructure datasets, determining reliable equipment-count distributions for each facility stratum requires scanning a large fraction of sites within the basin. For example, if larger, high-equipment-count facilities within a stratum are oversampled, extrapolated emissions may be overestimated. Careful consideration of facility characteristics is therefore critical for generating representative basin-wide inventories.

Leveraging the detailed facility-level equipment information, we modified our Monte Carlo framework to use the distribution of equipment counts as the cumulative distribution function (CDF) from which facility draws were made. To construct this equipment-count CDF, we first categorized all unique facilities scanned throughout the entire measurement campaign by their respective stratum and then generated a representative CDF for each stratum (Figure 3A). For quarterly extrapolation to unmeasured sites, we used this global equipment-count

distribution derived from the cumulative campaign data. This approach ensures that the probability of drawing a given facility reflects the underlying distribution of facility equipment counts within each stratum, rather than assigning equal probability to all facilities. Without this weighting, results would depend more heavily on the specific sample measured and may not reflect the true composition of the facility population. This method relies on the assumption that while an individual quarter's scans may not fully represent the broader facility stratum population, aggregating equipment count data across the entire campaign provides a more representative characterization of each stratum. As campaign coverage expands, these distributions converge toward the true basin composition, improving the accuracy of quarterly extrapolations and improving planning of subsequent deployments, ultimately supporting unbiased scaling to the full facility population.

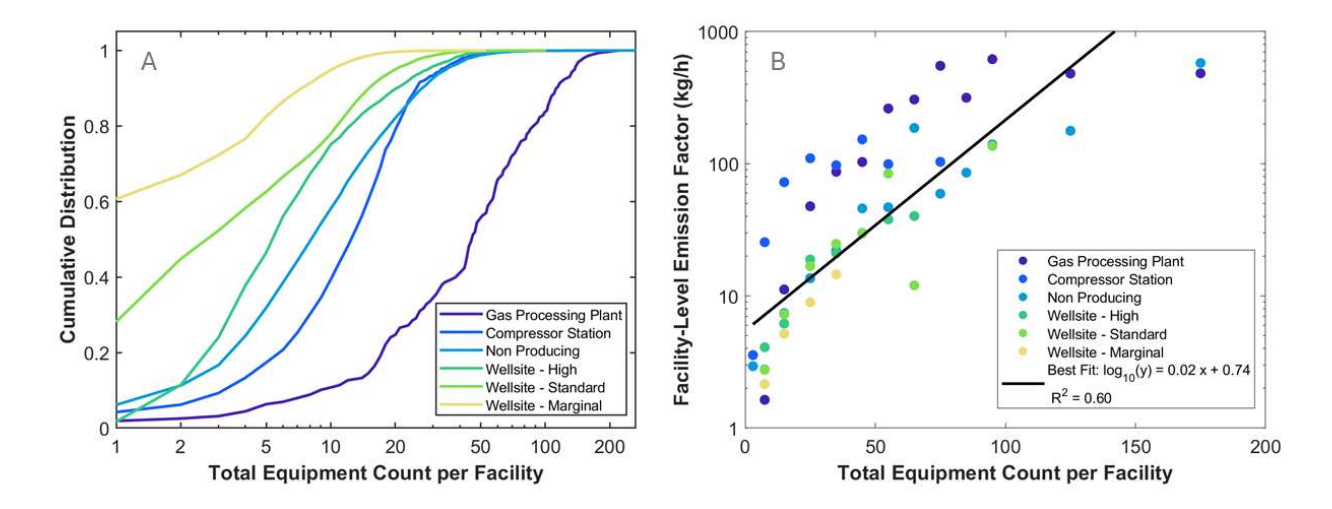


Figure 3. (A) Cumulative distribution function (CDF) of total equipment count per facility for each facility stratum across all unique sites surveyed over the four quarters. These CDFs were used in the Monte Carlo simulation to generate random draws for bootstrapping emissions. (B) Facility-level emission factor as a function of total equipment count per facility, grouped by facility stratum. Facilities were binned by total equipment count to calculate emission factors using variable-width bins with edges: [1, 5, 10, 20, 30, 40, 50, 60, 70, 80, 90, 100, 150, 200]. The black line represents the best-fit line derived from the binned data across all facility strata showing a strong correlation between equipment count and facility-level emission factor.

For each stratified Monte Carlo realization (N_{mc}), facilities within a given stratum were sampled with replacement using the equipment count-based CDF described above. The number of facilities drawn matches the total population size for that stratum(n_{strata}). Once a facility is selected, if there are associated emission sources they are retrieved and processed through the source-level GML quantification error model. The measured signal-to-noise ratio (SNR) of each detection is used as the input to generate a CDF of the relative error ratio (RER; measured emission rate divided by actual emission rate) for that specific source, which defines the average bias and uncertainty. A random value between 0 and 1 is then drawn from this CDF, and the corresponding bias-corrected emission rate is assigned to that source for the given

realization. This process is repeated across all strata, and the results are aggregated to produce total emissions estimates. These emissions represent the "measured emissions" component reported in the results. Over many Monte Carlo realizations, the source-level estimates converge to the average bias-corrected values defined by the RER distribution while also capturing the quantification uncertainty interval.

The so-called "missed emissions" are estimated within the Monte Carlo framework by inverting the GML probability of detection (PoD) model. The analysis focuses on emissions within GML's partial detection region (0.4 to 3 kg/h), where detection is probabilistic, to estimate both the number of undetected emitters and their magnitudes. To account for variations in deployment conditions across a measurement campaign, wind speed and measured gas concentration noise (GCN) values are randomly sampled with replacement. During each Monte Carlo realization, a wind speed and GCN value are randomly drawn and assigned to each emission in the partial detection region and input into the PoD model to determine the likelihood of detecting that emission under those conditions. The number of missed sources is estimated using the ratio of the probability of missing an emission to the probability of detecting one, estimating how many emissions go undetected for each one that is successfully detected. Finally, the CDF of the partial detection emission rates, scaled by the PoD, is used to estimate the distribution of missed emissions, from which the number of missed sources is randomly drawn with replacement. Through repeated realizations, this approach captures variability in the number of missed sources and the POD-scaled distribution, providing an estimate and confidence interval for the number and magnitude of emissions likely missed due to detection limitations. Further details and illustration of this method are provided in Section S2.3.

2.4 Natural Gas Gathering Line Emissions

Natural gas gathering lines were not directly targeted in the measurement campaign but contribute to total emissions and must be included to develop a comprehensive basin-wide inventory. We use emission factors derived from aerial surveys over the Permian Basin 22 , which report a wide range of values and a decreasing trend across four campaigns conducted between 2019 and 2021. We use the average emission factor from the latest two campaigns in 2021 and use the result that is reported for persistent emissions observed on multiple days. This results in an emission factor of 3.75 ± 1.8 Mg year⁻¹ km⁻¹. In applying these factors, we assume that the estimated emission factor is complete, and the uncertainty is accurately captured. Using the Rextag natural gas pipeline database, we identified 141,999 km of operational gathering lines in the Permian Basin, with 106,912 km in Texas and 35,087 km in New Mexico. This corresponds to estimated emissions of 532.5 ± 255.6 kt/year basin-wide, including 400.9 ± 192.4 kt/year in Texas and 131.6 ± 63.2 kt/year in New Mexico.

3 Results

This 2024 measurement campaign resulted in comprehensive methane emission inventories for the Permian Basin (Section 3.1), defined spatially using the U.S. Energy Information Administration (EIA) boundary. Separate inventories were produced for the Texas and New Mexico portions of the basin (Section 3.2). The dataset also enabled complete inventories for 15 of the top producers in the basin (Section 3.3), supporting operator performance benchmarking.

3.1 Basin Inventory

Total emissions from the Bridger campaign were estimated on a quarterly basis, with results summarized in Figure 4A and Table 2. The average quarterly emission rate based on the measurement campaign was 1,139 kt CH₄ and ranged from 1,056 to 1,233 kt CH₄, with quarter-specific 95% confidence intervals that on average extended from –22% to +33% of each estimate. Quarterly results were highly consistent, with overlapping 95% confidence intervals and stable proportions of missed emissions, highlighting the consistency of the measurement and modeling approach and basin-level emissions on quarterly time scales. Winter quarters (Q1 and Q4) were up to 17% higher than summer quarters (Q2 and Q3), aligning with the 18% increase reported by Hu et al.²³, whereas TROPOMI satellite observations suggest a larger 60% seasonal increase.²⁴ Aggregating the quarterly Bridger inventory (Figure 4B), the annualized emissions were 4,555 kt CH₄ (95% CI: 3,533 to 5,718 kt).

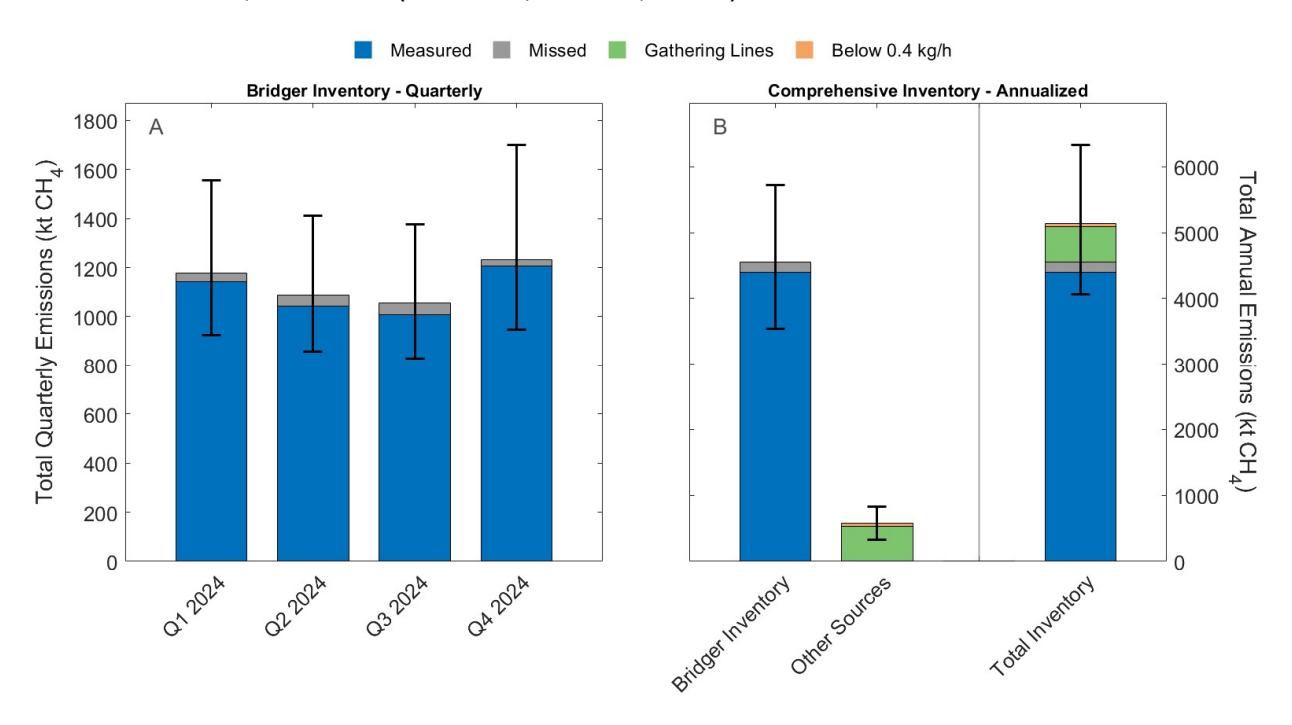


Figure 4. Methane emissions from the Permian Basin. (A) Quarterly measured and estimated missed emissions based on the Bridger measurement campaign. (B) Annualized Bridger inventory with added gathering line emissions and sources below 0.4 kg/h, representing the lower bound of the Bridger inventory. Error bars indicate 95% confidence intervals.

To translate inventory totals into actionable mitigation, attribution by facility and equipment type is essential for targeted strategies. Figure 5 summarizes this breakdown by facility stratum and equipment type. Non-producing facilities were the largest contributor (38%), reflecting both their large site counts and the prevalence of tank and processing equipment. Standard and marginal producing wellsites contributed 19% and 14%, respectively. Compressor stations and gas processing plants each contributed 11% despite relatively high emission factors because their populations were smaller, and high producing wellsites contributed the least. At the equipment level, tanks (31%) and compressors (28%) dominated and together accounted for 59% of total emissions, highlighting primary mitigation opportunities. Flares comprised 15%, other sources not linked to a major equipment type accounted for 14% (for example, completions or hydraulic fracturing), and separators, wells, and vapor recovery units contributed 9%, 3%, and 0.2%, respectively.

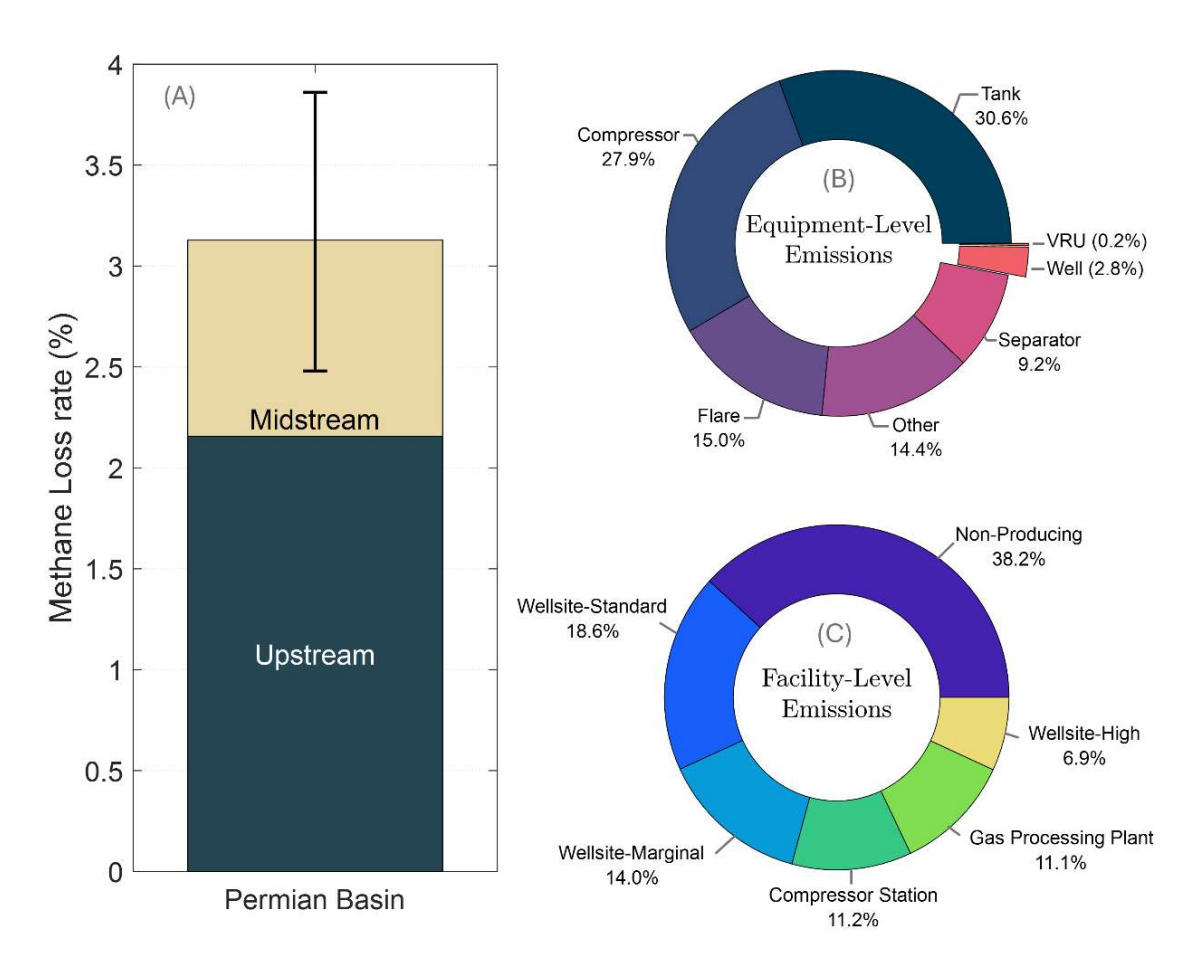


Figure 5. (A) Basin-wide methane loss rate partitioned into upstream and midstream sectors with 95% confidence interval. (B) Equipment-level and (C) facility-level breakdowns of total emissions for the Bridger campaign, where donut segments indicate each category's percent contribution to total emissions.

To construct the comprehensive inventory, we augmented the Bridger facility-level inventory with gathering line emissions and an estimate of sources below the 0.4 kg/h inventory

threshold. Gathering line emissions totaled 532 kt CH₄ (95% CI: 277–788 kt; green, Figure 4B). Sub-threshold emissions were estimated using data from a 2019 to 2021 study that combined a less sensitive aerial technology for detecting large emission sources with emissions modeling for smaller sources in an attempt to produce a complete emissions distribution for the Permian Basin.⁹ Sources below 0.4 kg h⁻¹ were estimated to contribute about 1% of total basin-wide emissions. Assuming the gathering line estimate is complete, the Bridger inventory captured 99% of total emissions, and we therefore added 1% (46 kt CH₄; orange, Figure 4B) to represent sub-threshold sources. Combining these components resulted in a comprehensive inventory of 5,133 kt CH₄ for 2024 (95% CI: 4,070–6,337 kt).

Methane intensity was calculated in two forms: loss rate, the ratio of methane emissions to methane in produced natural gas, and NGSI intensity, defined by the Natural Gas Sustainability Initiative as methane emissions relative to total energy produced from oil and gas. We conservatively use a methane fraction of 0.90 in produced gas, and additional details on these calculations are provided in the supporting information. For upstream and midstream facilities combined, the total loss rate was 3.13% (Figure 5A), and the NGSI intensity was 1.31% (Table 2). NGSI intensity is lower because the Permian Basin produces a large share of oil relative to gas; in gas dominant basins such as the Haynesville, the two metrics would be nearly identical. Segment specific results show upstream emissions (wellsites and non-producing sites) having a loss rate of 2.16% and an NGSI intensity of 0.91%. The facility- and segment-level resolution of this inventory enables its direct application to supply-chain methane-intensity and life-cycle assessment frameworks by linking emissions to specific production and transport stages.

3.2 State-Level Inventory

Texas, consistent with its larger share of gas production, accounts for the majority of basin emissions. Annualized emissions were 4,038 kt CH_4 yr⁻¹ for Texas (95% CI: –21% to +24%), representing 79% of the basin emissions and 68% of basin gas production. New Mexico contributed 1,095 kt CH_4 yr⁻¹ (95% CI: –21% to +23%), or 21% of the basin emissions, with 32% of basin gas production (Table 2). Segment attribution shows that upstream sources contribute 71% of Texas emissions (2,871 kt CH_4 yr⁻¹) and 61% of New Mexico emissions (668 kt CH_4 yr⁻¹), with the remainder from midstream (29% in Texas and 39% in New Mexico). Variations between state emission shares and productions may reflect differences in infrastructure mix, operational practices, production growth rates, and policy.

Table 2. Methane loss rate, NGSI intensity, methane emission factor²⁵, total 2024 annualized emissions, and oil and gas production for the Permian Basin, Texas, and New Mexico, reported for both combined upstream and midstream facilities and for upstream facilities only.

Segment	Area	Total Emissions (kt CH ₄ / yr)	95% CI (relative)	Loss Rate (%)	NGSI Intensity (%)	Emission Factor (g/MJ)	Gas Production (Bcf/d)	Oil Production (Mbbl/d)
	Permian	5,133	[-21%, +23%]	3.13	1.31	0.21	26.0	6,312.7
Upstream &	Texas	4,038	[-21%, +24%]	3.60	1.51	0.24	17.8	4,314.8
Midstream	New Mexico	1,095	[-21%, +23%]	2.10	0.89	0.14	8.2	1,998.0
	Permian	3,539	[-17%, +23%]	2.16	0.91	0.15	26.0	6,312.7
Upstream	Texas	2,871	[-17%, +23%]	2.56	1.08	0.17	17.8	4,314.8
оржени	New Mexico	668	[-15%, +20%]	1.28	0.54	0.09	8.2	1,998.0

The 2024 New Mexico loss rate for midstream and upstream was 2.1%. The state's 2026 rule targets 98% gas capture, equivalent to a 2% loss rate, putting New Mexico near the target level. Texas exhibits a loss rate of 3.6% (NGSI intensity 1.51%). These state-level patterns are consistent with findings reported by Varon et al. (2025).²⁴

To contextualize the New Mexico loss rate, we compare New Mexico emission factors to Permian-wide values and find they are lower across most equipment and facility categories (Figure 6). At the equipment level, New Mexico is lower for every category except VRUs, with the largest gaps for flares, separators, and wells, and clear differences for tanks and compressors. These equipment-level patterns carry through to facilities, where gas processing plants, non-producing sites, and standard producing wellsites show lower factors. The facility-and equipment-level granularity of this work shows New Mexico's lower intensity is broadbased across source categories and is not driven by a single source. Further investigation will be required to determine the underlying causes for lower emission factors, which may include differences in facility production rate and composition, equipment age, infrastructure configuration, and operating practices.

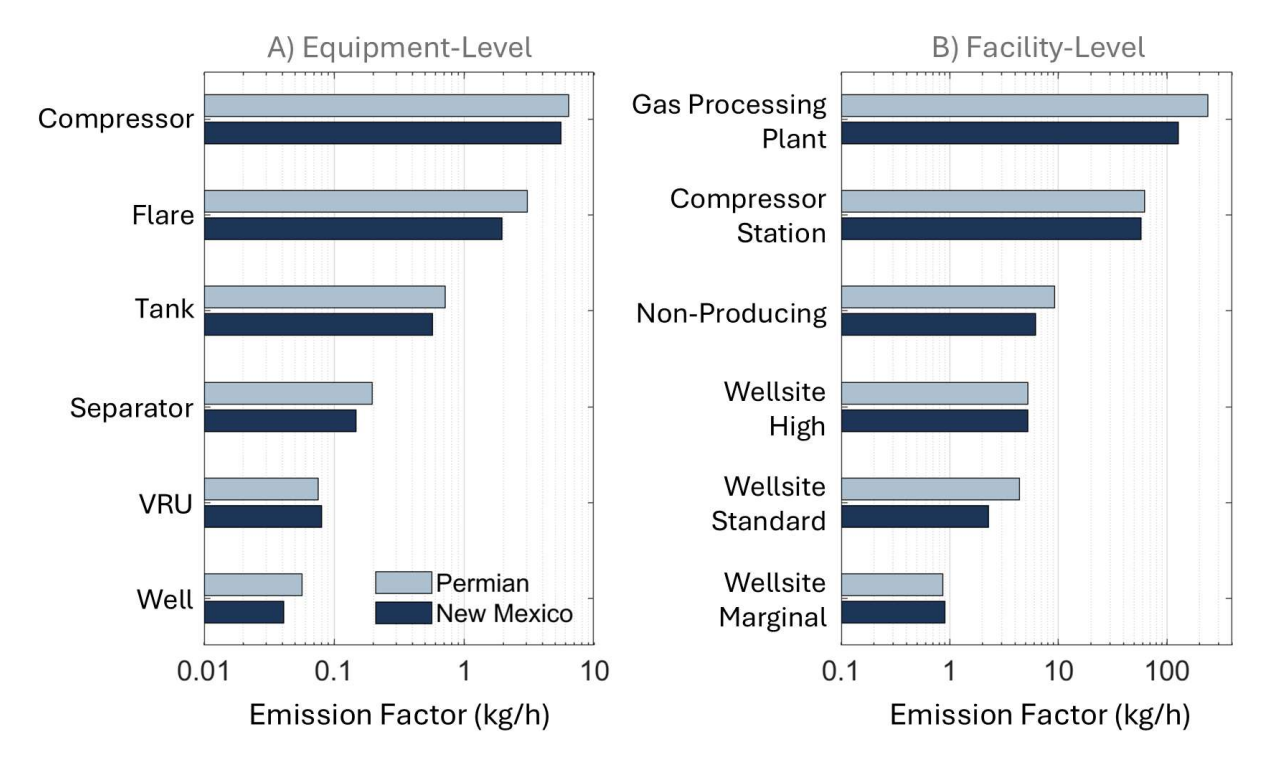


Figure 6. Measurement-based methane emission factors are shown for the Permian Basin (light blue) and the New Mexico portion of the Permian (dark blue) at the equipment level (A) and facility level (B). Emission factors represent the average emission rate per equipment unit or facility type, including zeros, with the x-axis displayed on a logarithmic scale.

3.3 Top-Producing Operators

 We developed annualized, operator-level inventories for 15 Permian Basin operators where facility sampling coverage was sufficient relative to the population. Facility counts and produced gas volumes were compiled from Enverus. This set is not intended to match the top fifteen producers by output, yet it includes several of the largest operators in the basin and together they account for approximately 79% of basin gas production. All results are presented with anonymized operator identifiers (Figure 7). To enable fair comparison across companies, we report upstream methane loss rates only. Midstream footprints vary widely by operator and would confound direct comparisons if included.

Many high producing operators in this cohort perform well below the Permian Basin upstream average, often by a wide margin, with a cohort loss rate average of 0.93%. The basin average is generally pulled upward by smaller operators that manage large numbers of marginal wellsites. Marginal wells typically exhibit higher emissions intensity. ¹⁹ Larger operators tend to operate newer equipment and higher-throughput sites and have greater resources for emissions monitoring and mitigation, which helps explain their lower loss rates. This operator-resolved, measurement-based approach enables granular peer comparisons within a basin, facilitating the identification and sharing of best practices. It also provides a practical pathway

for OGMP 2.0 reporting and continuous benchmarking of progress toward methane reduction goals.

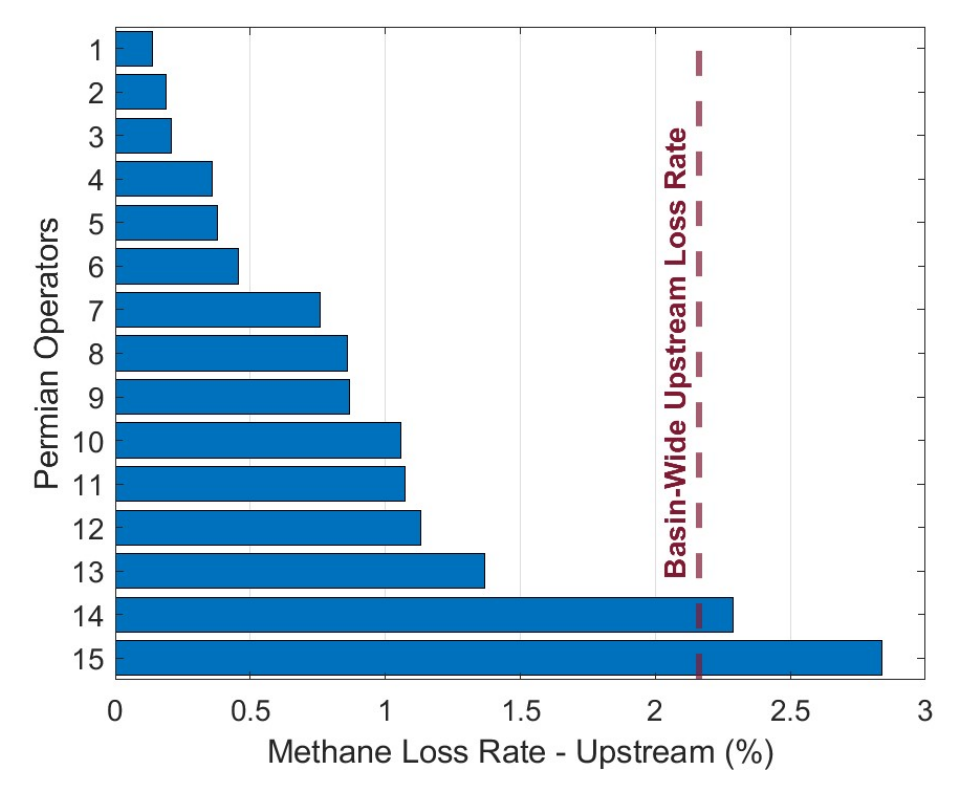


Figure 7. Upstream methane loss rates (%) for 15 Permian Basin operators derived from the 2024 aerial campaign. The operators represent some of the largest in the basin, though the set may not correspond exactly to the top 15 by production. The dashed vertical line marks the Permian Basin average upstream loss rate.

4 Discussion

4.1 Comparison with Previously Published Inventories

Figure 8 places our 2024 estimated methane loss rate alongside basin-level estimates reported since 2019 and overlays average daily gas production.^{7,9,24,26–28} While not every study covers the entire Permian, each includes both upstream and midstream sources, and all values are harmonized to a methane fraction of 0.9 for comparability. Our estimate is consistent with loss rates from these prior studies derived from measurements at varying scales. The series shows relatively stable or slightly declining intensity since 2019, during a period of increasing gas production, suggesting progress in efficiency and mitigation.

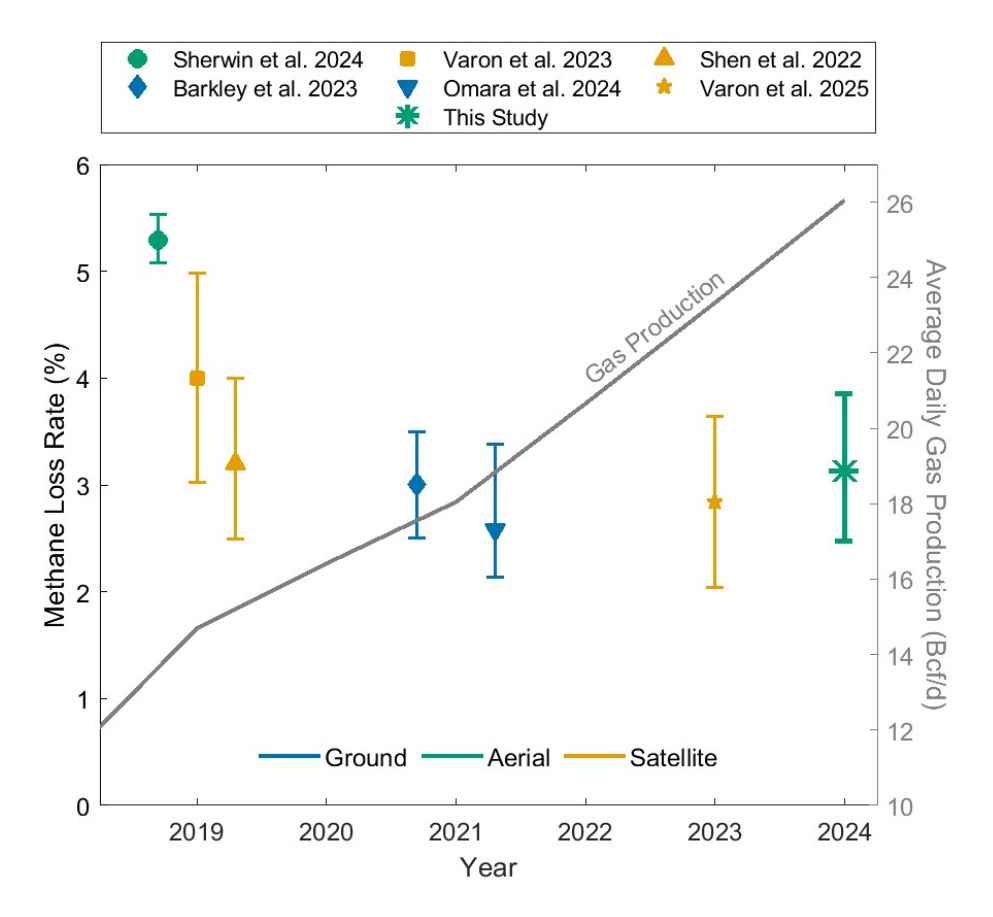


Figure 8. Permian Basin methane loss rate estimates by study with confidence intervals, plotted by year on the left axis. Average daily gas production (Bcf/d) is shown as a gray line on the right axis. Color denotes measurement scale: blue ground-based, green aerial, and orange satellite. Additional details on the studies in this comparison are in Section SI5. All loss rates are harmonized to a methane fraction of 0.90 in produced gas, with values rescaled where other fractions were assumed.

4.2 Implications for Basin Wide Benchmarking and OGMP Reporting

A low detection sensitivity, equipment level workflow that directly captures about 99% of total emissions delivers inventories that are immediately actionable. By tying each plume to specific equipment within a facility, totals become concrete worklists for maintenance, repair, and capital planning rather than abstract basin averages. In contrast, inventories built from less sensitive aerial systems or from space-based observations leave large gaps. Given the measured emission rate distribution, a system with a 25 kg/h sensitivity would capture only 60% of basin emissions, and a system near 100 kg/h, typical of satellite point source imagers, would capture only 31%. The remainder must be simulated rather than measured, undermining credible basin comparison and removing the possibility to measure improvements in the simulated portions. Closing this sensitivity gap is essential for reliable benchmarking across operators and basins.

The workflow produces an equipment level inventory consistent with OGMP Level 4 and a site level inventory consistent with OGMP Level 5. Because results aggregate transparently

from equipment to facility to operator to basin, with uncertainty reported in a consistent format, the method supports defensible and cost-effective benchmarking, target setting, and verification across reporting periods and peers.

4.3 Model Limitations and Assumptions

The primary limitation of this approach is temporal coverage. The method assumes that broad spatially representative sampling, paired with snapshot measurements across many sites, captures the native frequency of emission events by source type. This allows the Monte Carlo framework to explore plausible temporal variability. The ergodic principle is often invoked, which states that the ensemble average of random samples at many sites equals the time averaged total emissions when sites are sufficiently homogeneous. However, ergodicity alone is not sufficient. Without representative sampling, one could place a continuous monitor at a single wellsite and, by adhering to ergodicity principle, extrapolate its measurements to all similar sites. That would be inappropriate because it ignores spatial heterogeneity and operational diversity that materially affect emissions.

A recent study explored the question of how sensitive an inventory is to reasonable methodological choices and showed that aerial based inventories remain relatively stable across extrapolation methods, whereas point sensor network inventories vary substantially and are especially sensitive to spatial extrapolation ²⁹. This sensitivity reinforces the earlier point that ergodicity by itself is not a sound assumption because a single or sparse network of continuous monitors cannot be reliably scaled to a basin without representative spatial sampling.

Reliability depends on balanced coverage across three dimensions: temporal coverage, spatial coverage, and detection sensitivity. This study addresses spatial coverage and detection sensitivity strongly, while temporal remains as the largest potential for minimizing potential systematic error. Nevertheless, we implemented quarterly measurements to capture seasonal differences, an approach rarely used in prior aerial inventories, while recognizing that quarterly sampling still cannot resolve all short-lived operational upsets between flights. Even so, the campaign maintained a consistent presence. In 2024, sensors were in the air on 195 days, averaging 2.7 sensors per flown day and accumulating 2,252 flight hours. Rather than a brief concentrated flight period, this cadence kept GML observing somewhere in the basin on more than half the days of the year, providing substantially broader temporal presence than prior campaigns concentrated into narrow windows.

A related temporal limitation is the lack of nighttime scans. Continuous tower observations indicate that daytime and nighttime emissions can differ by as much as 27% in the Permian.³⁰ Because our campaign focused on daytime flights, diurnal variability may be under sampled, which could bias the inventory if nighttime conditions systematically lower emissions. Unlike sunlight-based aerial detection systems, GML is a lidar and can be operated at night, so future work will include nocturnal flights to characterize and correct for diurnal effects.

A secondary limitation of this work is that we did not account for wind speed errors from the HRRR model, which we used to estimate fluxes. Recent work by Conrad and Johnson showed that errors in modeled winds can be correlated across space and time.³¹ If wind speed bias is present and error correlation is not accounted for, inventories can be biased and their reported uncertainty understated, because correlated errors do not average down with more samples. They recommend practical steps such as leaving more than two days between repeat measurements at the same site and shifting revisit times by about six hours to reduce daily wind correlations. In our Permian campaign we did not conduct site revisits, but instead, sampling was spread over many weeks and in different areas within each quarter, and across four quarters. This sampling strategy introduces multi-day to multi-month lags, which should limit correlated wind error and bias, even though we did not explicitly model wind error correlation here.

Finally, the population of non-producing sites was estimated using the ML approach with targeted manual verification described above and detailed in the SI. Because non-producing sites account for a large share of facility-level emissions, the accuracy of this population estimate is critically important. Although we developed what we believe is the best available estimate, more complete infrastructure reporting would further reduce uncertainty. For example, Canadian provincial databases provide detailed facility types and functions, enabling more accurate population counts and finer stratification for extrapolation. ^{8,10} Adopting similarly granular, routinely updated reporting standards in the United States would materially improve the fidelity and accountability of methane inventories.

5 Conclusion

This study produces a high-resolution, source-resolved methane inventory for the 2024 Permian Basin that is both comprehensive and actionable. Quarterly aerial LiDAR scans across 51,770 facilities, paired with an equipment-weighted Monte Carlo framework, capture an estimated 99% of basin emissions down to 0.4 kg/h and quantify them with transparent characterized uncertainty. The resulting annualized total is 5,133 kt CH₄ with a basin-wide methane loss rate of 3.13%, and the method resolves emissions to equipment and facility so operators can act. Non-producing sites carry a large share, and tanks and compressors dominate equipment-level contributions, turning basin totals into clear mitigation priorities (Figure 5). State-level analysis indicates New Mexico is already near its 2026 2% loss rate target (Figure 6 and Table 2). Seasonal variation was observed, with winter about 17% higher than summer (Figure 4A). Together these results establish a credible baseline for year-over-year benchmarking and a transferable framework to produce accurate inventories for other U.S. basins and operators pursuing OGMP 2.0 Gold Standard.

Conflict of Interest Disclosure

- 556 Bridger Photonics, Inc. profits from sales of Gas Mapping LiDAR methane emissions monitoring
- 557 services.

555

558

565

Acknowledgments

- 559 Bridger Photonics, Inc. thanks ARPA-E and the Montana Board of Research and
- 560 Commercialization Technology for support in developing the Gas Mapping LiDAR hardware. We
- also acknowledge the Bridger Photonics Operations team for their exceptional work executing
- the field deployment and processing the LiDAR data throughout the campaign, and we thank
- Andrew Bartnik, Devin Goodwin, and Peter Ottsen for their support during the development of
- these workflows.

References

- U.S. Environmental Protection Agency. *EPA (2024) Inventory of U.S. Greenhouse Gas Emissions and Sinks: 1990-2022*; EPA 430-R-24-004; U.S. Environmental Protection Agency:
 Washington, DC, 2024. https://www.epa.gov/ghgemissions/inventory-us-greenhouse-gasemissions-andsinks-1990-2022 (accessed 2025-08-18).
- Shindell, D.; Ravishankara, A.; Kuylenstierna, J. C.; Michalopoulou, E.; Höglund-Isaksson, L.;
 Zhang, Y.; Seltzer, K.; Ru, M.; Castelino, R.; Faluvegi, G. *Global Methane Assessment:* Benefits and Costs of Mitigating Methane Emissions; 9280738542; United Nations
 Environment Programme, 2021.
- 574 (3) Fox, T. A.; Barchyn, T. E.; Risk, D.; Ravikumar, A. P.; Hugenholtz, C. H. A Review of Close-575 Range and Screening Technologies for Mitigating Fugitive Methane Emissions in Upstream 576 Oil and Gas. *Environ. Res. Lett.* **2019**, *14* (5), 053002. https://doi.org/10.1088/1748-577 9326/ab0cc3.
- Kutherford, J. S.; Sherwin, E. D.; Ravikumar, A. P.; Heath, G. A.; Englander, J.; Cooley, D.; Lyon, D.; Omara, M.; Langfitt, Q.; Brandt, A. R. Closing the Methane Gap in US Oil and Natural Gas Production Emissions Inventories. *Nat Commun* **2021**, *12* (1), 4715. https://doi.org/10.1038/s41467-021-25017-4.
- (5) Alvarez, R. A.; Zavala-Araiza, D.; Lyon, D. R.; Allen, D. T.; Barkley, Z. R.; Brandt, A. R.; Davis,
 K. J.; Herndon, S. C.; Jacob, D. J.; Karion, A.; Kort, E. A.; Lamb, B. K.; Lauvaux, T.;
 Maasakkers, J. D.; Marchese, A. J.; Omara, M.; Pacala, S. W.; Peischl, J.; Robinson, A. L.;
 Shepson, P. B.; Sweeney, C.; Townsend-Small, A.; Wofsy, S. C.; Hamburg, S. P. Assessment of
 Methane Emissions from the U.S. Oil and Gas Supply Chain. *Science* 2018, *361* (6398), 186–
 188. https://doi.org/10.1126/science.aar7204.
- 588 (6) https://www.ogmpartnership.org/our-member-companies. Membership, Oil and Gas 589 Methane partnership 2.0. https://www.ogmpartnership.org/our-member-companies 590 (accessed 2025-09-08).
- 591 (7) Omara, M.; Himmelberger, A.; MacKay, K.; Williams, J. P.; Benmergui, J.; Sargent, M.; Wofsy, S. C.; Gautam, R. Constructing a Measurement-Based Spatially Explicit Inventory of US Oil

- and Gas Methane Emissions (2021). *Earth Syst. Sci. Data* **2024**, *16* (9), 3973–3991. https://doi.org/10.5194/essd-16-3973-2024.
- Johnson, M. R.; Conrad, B. M.; Tyner, D. R. Creating Measurement-Based Oil and Gas
 Sector Methane Inventories Using Source-Resolved Aerial Surveys. *Commun Earth Environ* **2023**, *4* (1), 139. https://doi.org/10.1038/s43247-023-00769-7.
- (9) Sherwin, E. D.; Rutherford, J. S.; Zhang, Z.; Chen, Y.; Wetherley, E. B.; Yakovlev, P. V.;
 Berman, E. S. F.; Jones, B. B.; Cusworth, D. H.; Thorpe, A. K.; Ayasse, A. K.; Duren, R. M.;
 Brandt, A. R. US Oil and Gas System Emissions from Nearly One Million Aerial Site
 Measurements. *Nature* 2024, 627 (8003), 328–334. https://doi.org/10.1038/s41586-024-07117-5.
- (10) Conrad, B. M.; Tyner, D. R.; Li, H. Z.; Xie, D.; Johnson, M. R. A Measurement-Based
 Upstream Oil and Gas Methane Inventory for Alberta, Canada Reveals Higher Emissions
 and Different Sources than Official Estimates. *Commun Earth Environ* 2023, *4* (1), 416.
 https://doi.org/10.1038/s43247-023-01081-0.
- (11) Brown, J. A.; Moy, M.; Santos, A.; Rimelman, E.; Khaliukova, O.; Okenberg, C.; Daniels, W.
 S.; Hammerling, D. M.; Zimmerle, D.; Hodshire, A. L. *Colorado Ongoing Basin Emissions* (COBE) Final Report; Colorado State University Energy Institute; Colorado School of Mines:
 Fort Collins, CO; Golden, CO, 2025.
- 611 (12) Bridger Photonics, Inc. *Characterization of Emission Source Localization Accuracy for*612 *Bridger Photonics' Gas Mapping LiDAR*; White Paper; 2024.
- (13) Thorpe, M. J.; Kreitinger, A. T. Apparatuses and Methods for Gas Flux Measurements. US12066353B2, August 20, 2024.
- (14) Bell, C.; Rutherford, J.; Brandt, A.; Sherwin, E.; Vaughn, T.; Zimmerle, D. Single-Blind
 Determination of Methane Detection Limits and Quantification Accuracy Using Aircraft Based LiDAR. *Elementa: Science of the Anthropocene* 2022, 10 (1), 00080.
 https://doi.org/10.1525/elementa.2022.00080.
- (15) Conrad, B. M.; Tyner, D. R.; Johnson, M. R. Robust Probabilities of Detection and
 Quantification Uncertainty for Aerial Methane Detection: Examples for Three Airborne
 Technologies. Remote Sensing of Environment 2023, 288, 113499.
 https://doi.org/10.1016/j.rse.2023.113499.
- (16) Thorpe, M. J.; Kreitinger, A.; Altamura, D. T.; Dudiak, C. D.; Conrad, B. M.; Tyner, D. R.;
 Johnson, M. R.; Brasseur, J. K.; Roos, P. A.; Kunkel, W. M. Deployment-Invariant Probability
 of Detection Characterization for Aerial LiDAR Methane Detection. *Remote Sensing of Environment* 2024, 315, 114435.
- (17) Dudiak, C. D.; Goodwin, D. B.; Altamura, D. T.; Donahue, C. P.; Thorpe, M. J. Quantification
 Error Model for Aerial LiDAR Methane Emission Rate Estimates. *Manuscript In Preparation* 2025.
- (18) Thorpe, M.; Krietinger, A.; Altamura, D.; Dudiak, C.; Conrad, B.; Tyner, D.; Johnson, M.;
 Brasseur, J.; Roos, P.; Kunkel, W.; Carre-Burritt, A.; Abate, J.; Price, T.; Yaralian, D.; Kennedy,
 B.; Newton, E.; Rodriguez, E.; Ibrahim Elfar, O.; Zimmerle, D. Deployment-Invariant
 Probability of Detection Characterization for Aerial LiDAR Methane Detection.
 Environmental Monitoring January 26, 2024. https://doi.org/10.31223/X5R96M.

- (19) Omara, M.; Zavala-Araiza, D.; Lyon, D. R.; Hmiel, B.; Roberts, K. A.; Hamburg, S. P. Methane
 Emissions from US Low Production Oil and Natural Gas Well Sites. *Nat Commun* 2022, *13*(1), 2085. https://doi.org/10.1038/s41467-022-29709-3.
- 638 (20) Ester, M.; Kriegel, H.-P.; Sander, J.; Xu, X. A Density-Based Algorithm for Discovering Clusters 639 in Large Spatial Databases with Noise; 1996; Vol. 96, pp 226–231.
- (21) Omara, M.; Gautam, R.; O'Brien, M. A.; Himmelberger, A.; Franco, A.; Meisenhelder, K.;
 Hauser, G.; Lyon, D. R.; Chulakadabba, A.; Miller, C. C.; Franklin, J.; Wofsy, S. C.; Hamburg, S.
 P. Developing a Spatially Explicit Global Oil and Gas Infrastructure Database for
 Characterizing Methane Emission Sources at High Resolution. *Earth Syst. Sci. Data* 2023, 15
 (8), 3761–3790. https://doi.org/10.5194/essd-15-3761-2023.
- Yu, J.; Hmiel, B.; Lyon, D. R.; Warren, J.; Cusworth, D. H.; Duren, R. M.; Chen, Y.; Murphy, E.
 C.; Brandt, A. R. Methane Emissions from Natural Gas Gathering Pipelines in the Permian
 Basin. *Environ. Sci. Technol. Lett.* 2022, *9* (11), 969–974.
 https://doi.org/10.1021/acs.estlett.2c00380.
- (23) Hu, L.; Andrews, A. E.; Montzka, S. A.; Miller, S. M.; Bruhwiler, L.; Oh, Y.; Sweeney, C.; Miller,
 J. B.; McKain, K.; Ibarra Espinosa, S. An Unexpected Seasonal Cycle in US Oil and Gas
 Methane Emissions. *Environmental Science & Technology* 2025, *59* (20), 9968–9979.
- (24) Varon, D. J.; Jacob, D. J.; Estrada, L. A.; Balasus, N.; East, J.; Pendergrass, D. C.; Chen, Z.;
 Sulprizio, M. P.; Omara, M.; Gautam, R. Seasonality and Declining Intensity of Methane
 Emissions from the Permian and Nearby US Oil and Gas Basins. 2025.
- (25) Johnson, M. R.; Conrad, B. M.; Zimmerle, D. J.; Kleinberg, R. L. Methane by the Numbers: The Need for Clear and Comparable Methane Intensity Metrics. EarthArXiv 2025.
- (26) Barkley, Z.; Davis, K.; Miles, N.; Richardson, S.; Deng, A.; Hmiel, B.; Lyon, D.; Lauvaux, T.
 Quantification of Oil and Gas Methane Emissions in the Delaware and Marcellus Basins
 Using a Network of Continuous Tower-Based Measurements. *Atmos. Chem. Phys.* 2023, 23
 (11), 6127–6144. https://doi.org/10.5194/acp-23-6127-2023.
- (27) Shen, L.; Gautam, R.; Omara, M.; Zavala-Araiza, D.; Maasakkers, J. D.; Scarpelli, T. R.;
 Lorente, A.; Lyon, D.; Sheng, J.; Varon, D. J.; Nesser, H.; Qu, Z.; Lu, X.; Sulprizio, M. P.;
 Hamburg, S. P.; Jacob, D. J. Satellite Quantification of Oil and Natural Gas Methane
 Emissions in the US and Canada Including Contributions from Individual Basins. *Atmos. Chem. Phys.* 2022, *22* (17), 11203–11215. https://doi.org/10.5194/acp-22-11203-2022.
- (28) Varon, D. J.; Jacob, D. J.; Hmiel, B.; Gautam, R.; Lyon, D. R.; Omara, M.; Sulprizio, M.; Shen,
 L.; Pendergrass, D.; Nesser, H.; Qu, Z.; Barkley, Z. R.; Miles, N. L.; Richardson, S. J.; Davis, K.
 J.; Pandey, S.; Lu, X.; Lorente, A.; Borsdorff, T.; Maasakkers, J. D.; Aben, I. Continuous
 Weekly Monitoring of Methane Emissions from the Permian Basin by Inversion of
 TROPOMI Satellite Observations. *Atmos. Chem. Phys.* 2023, 23 (13), 7503–7520.
 https://doi.org/10.5194/acp-23-7503-2023.
- (29) Fosdick, B. K.; Weller, Z.; Wong, H. X.; Corbett, A.; Roell, Y.; Martinez, E.; Berry, A.;
 Gielczowski, N.; Hajny, K. D.; Moore, C. Extrapolation Approaches for Creating
 Comprehensive Operator-Level Measurement-Based Methane Emissions Inventories.
 2025.
- 676 (30) Barkley, Z.; Davis, K. J.; Miles, N.; Richardson, S. J. Examining Daily Temporal Characteristics 677 of Oil and Gas Methane Emissions in the Delaware Basin Using Continuous Tower

678	Observations. Journal of Geophysical Research: Atmospheres 2025, 130 (6),
679	e2024JD042050.
680	(31) Conrad, B. M.; Johnson, M. R. Accounting for Spatiotemporally Correlated Errors in Wind
681	Speed for Remote Surveys of Methane Emissions. EGUsphere 2025, 2025, 1–31.
682	

683	Supporting Information for	
684	Aerial LiDAR-Based, Source-Resolved Methane Emissions Inventory: Perm	ian
385	Basin Case Study for Benchmarking U.S. Emissions	
686		
687 688 689	Christopher P. Donahue*, Kabir Oberoi, James W. Dillon, Vickira Hengst, Brandon Kennedy, Willian Kearney, Jackson Lennox, Elizabeth Rehbein, Rory Sykes, Cameron D. Dudiak, Dominic T. Altamuro Gabriel Doherty, Peter A. Roos, Jason K. Brasseur, and Michael J. Thorpe*	
690	Bridger Photonics, Inc., Bozeman, MT 59715, USA	
691	*Corresponding Authors	
692	Email: Christopher.Donahue@bridgerphotonics.com and Mike.Thorpe@bridgerphotonics.com	
693	Contents	
694	S1. Aerial measurement campaign planning	26
395	S1.1 Active oil and gas infrastructure population	26
696	S1.2 Non-producing facility population estimate	26
697	S1.3 Allocation of measurement sample	27
698	S2. Total emissions estimate and model framework details	29
699	S2.1 Snapshot emission rate distribution	29
700	S2.2 Measured emissions component	30
701	S2.3 Missed emissions component	30
702	S2.4 Error sources	32
703	S2.4.1 Extrapolation error	33
704	S2.4.2 Sample error	34
705	S2.4.3 Quantification error	34
706	S2.4.4 Detection sensitivity error	35
707	S3. Detection sensitivity achieved during the campaign	35
708	S4. Measured emissions distributions	36
709	S5. Measurement-based emissions factors	37
710	S5.1 Facility-level	38
711	S5.2 Equipment-level	38
712	S6. Previously published inventories	39
713	S7. Methane emission intensity calculation	39
714	S8. References	40

S1. Aerial measurement campaign planning

- 717 Developing a measurement-based inventory requires representative sampling because we
- 718 extrapolate measured emissions both spatially and temporally. We summarize only
- 719 implementation details here and refer readers to the Campaign Planning section of the main
- 720 manuscript for the overview and motivations (section 2.2).

716

721

732

733

734

735

736

737

738739

740

741

742

743

744

745

746

747

748

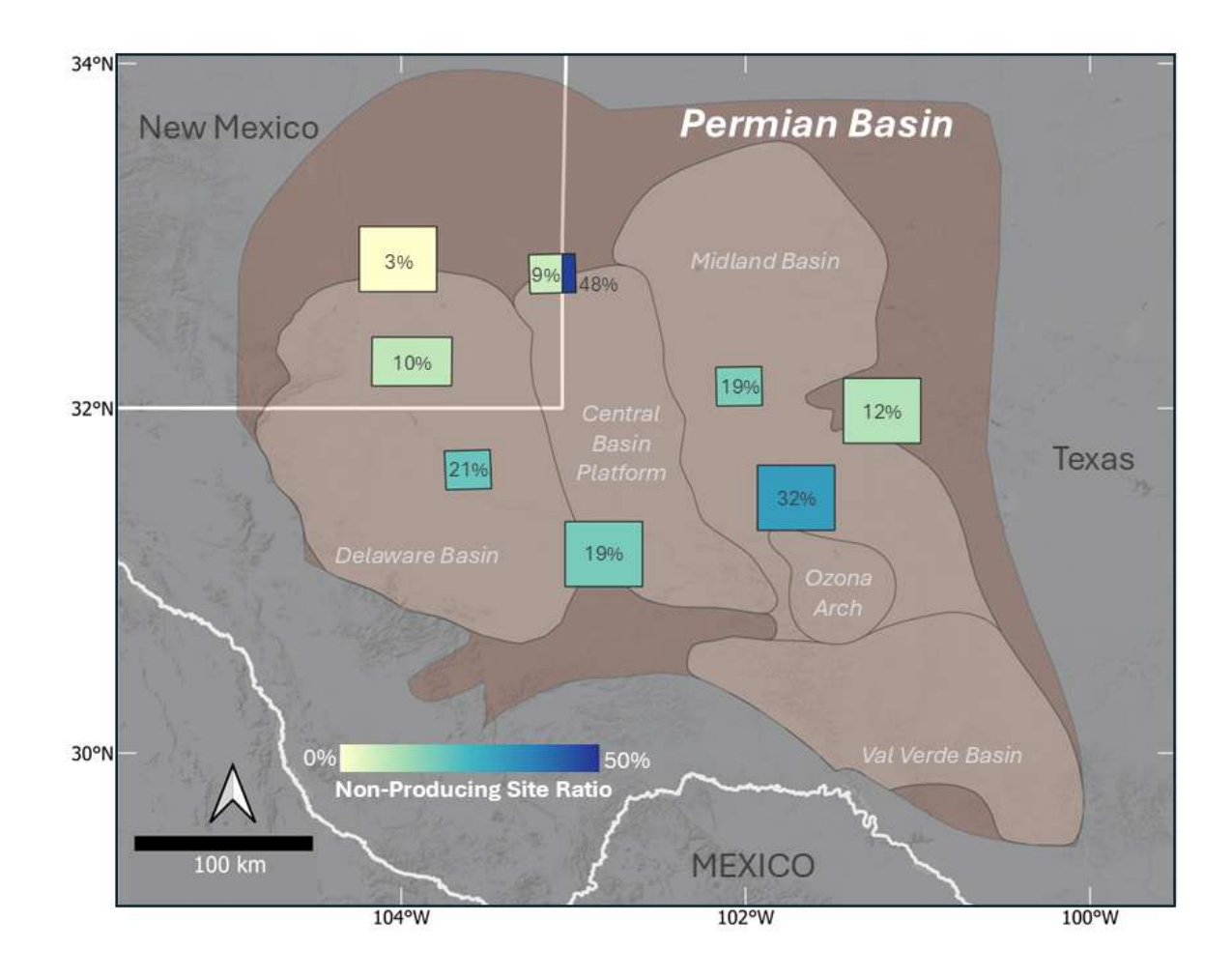
S1.1 Active oil and gas infrastructure population

- 722 Facility strata and production classes (high > 300 boed; standard 15–300 boed; marginal < 15
- boed) follow the main manuscript. We derived the basin population from the Rextag database,
- filtered wells to active and producing statuses, and clustered well pins to facilities using DBSCAN
- 725 with a 50 m radius. Midstream counts (gas plants, compressor stations, gas storage) were taken
- 726 directly from Rextag. Gathering and transmission compressors and gas storage were combined
- due to similar emission profiles and small populations. Where wells are co-located with a larger
- 728 facility, stratification follows the facility class with the highest expected emissions, as
- determined from historical emissions observed in prior GML scans for each facility class. Note
- 730 that public infrastructure data lack equipment-level counts, which motivates our equipment-
- 731 weighted extrapolation method described in the main text.

S1.2 Non-producing facility population estimate

We applied a machine-learning pad-detection model to 0.6 m NAIP (2022) imagery to generate pad polygons representing candidate non-producing sites, then excluded any polygons that intersected previously stratified upstream or midstream sites to avoid double-counting. These polygons served two purposes: they defined the non-producing site class population used in our stratification, and they informed flight planning. We performed manual quality checks (QC) on every non-producing facility sampled to be scanned and over nine geographically distributed polygons selected to span high- and low-activity areas, multiple formations, and coverage in both New Mexico and Texas (Figure S2). For each QC polygon, we computed the fraction of non-producing sites relative to active wellsites and then averaged across polygons to obtain a basin-wide share of 19.2% (range 3–48%). Applying this fraction to the count of active producing wellsites produced an estimated 21,613 non-producing sites across the basin.

While this provides a reasonable estimate of the non-producing site population, this stratum introduces uncertainty into the final inventory. For example, using the interquartile range of these estimates (9.5% to 26.5%) and the contribution of non-producing sites to total emissions, we estimate that this introduces approximately $\pm 17\%$ uncertainty in the total emissions estimate relative to the 19.2% non-producing site fraction used in the inventory.



Supplementary Figure 1. Map of the nine Permian subregions used to estimate the population of non-producing sites. Manual quality checks of machine learning-detected facility polygons were conducted in each subregion to assess classification accuracy and calculate the fraction of non-producing sites relative to active wellsites.

S1.3 Allocation of measurement sample

During the first three quarters, we used proportionate stratified sampling, allocating samples to each stratum in relative proportion to its population size to ensure representative coverage. Specifically, letting N_h be the population size of stratum h, $N = \sum_h N_h$ the total population, and n the total sample size, the allocation for each stratum, n_h was

$$n_h = n \frac{N_h}{N} \tag{S1}$$

Stratified sampling allocations remained relatively stable during this period.

To improve statistical efficiency, the quarter four sampling design adopted a Neyman allocation approach, which minimizes the variance of the overall estimator by distributing samples based on both the size and standard deviation of emissions in each stratum. With S_h denoting the within-stratum standard deviation (estimated from earlier quarters), the allocation is

$$n_h = n \frac{N_h S_h}{\sum_{j=1}^H N_j S_j} \tag{S2}$$

where j is a summation index running over all strata $(j=1,\ldots,H)$. In addition to statistical considerations, adjustments to the Neyman allocation were made based on emissions materiality. For example, greater sampling effort was directed toward compressor stations, gas processing plants, and newer high producing wellsites in the fourth quarter due to their large per-site contribution to total emissions. To support state-level representativeness checks, we break out the sample by state, quarter, and stratum in Table S1, complementing the campaign-wide quarterly totals shown in the main text.

 Future work should consider a modified Neyman allocation that incorporates both the standard deviation of emissions and the frequency or probability of detecting an emission event. This is particularly important when sample sizes are small. For instance, marginal wellsites may exhibit low variance and therefore receive limited sampling under standard Neyman allocation. However, if the probability of detecting an emission at these sites is only 10%, additional sampling is needed to adequately characterize the emission distribution for that stratum. This limitation is less significant for large-scale sampling.

Supplementary Table 3. Quarterly counts of facilities scanned in 2024 by state and facility stratum in the Permian Basin. Total Scanned is the sum of Q1-Q4 scan-visits (not necessarily unique facilities). Population is the estimated number of facilities in each stratum. Sampling Fraction = Total Scanned \div Population (values > 1 indicate multiple passes per facility on average). State totals (bottom rows) sum across strata and quarters.

State	Facility Stratum	Q1 2024	Q2 2024	Q3 2024	Q4 2024	Total Scanned	Population	Sampling Fraction
	Gas Processing Plant	28	26	28	158	240	188	1.28
	Compressor Station	205	214	203	457	1,079	541	1.99
	Non-Producing	1,770	1,569	1,629	1,046	6,014	16,775	0.36
Texas	Wellsite - High	1,346	1,489	1,479	1,250	5,564	4,358	1.28
	Wellsite - Standard	1,466	1,577	1,577	1,749	6,369	16,728	0.38
	Wellsite - Marginal	4,535	4,225	4,345	4,900	18,005	66,285	0.27
	Total Facilities (TX)	9,350	9,100	9,261	9,560	37,271	104,875	0.36
	Gas Processing Plant	14	19	18	50	101	54	1.87
	Compressor Station	156	147	138	277	718	398	1.80
	Non-Producing	620	565	545	241	1,971	4,837	0.41
New Mexico	Wellsite - High	1,202	1,277	1,260	552	4,291	2,451	1.75
IVICAICO	Wellsite - Standard	819	818	826	369	2,832	5,473	0.52
	Wellsite - Marginal	1,425	1,261	1,312	603	4,601	17,271	0.27
	Total Facilities (NM)	4,236	4,087	4,099	2,092	14,514	30,484	0.48

S2. Total emissions estimate and model framework details

S2.1 Snapshot emission rate distribution

Bridger source-level emissions data undergo pre-analysis processing to generate a snapshot emission rate distribution used in the Monte Carlo simulation. The term snapshot refers to a single point in time when aerial measurements are taken, without incorporating reflight data commonly used in LDAR operations to assess source persistence. Because Bridger cannot deploy GML sensors to all potential emission locations simultaneously, we treat the first observation of each emission location within a given quarter as its emission state for the snapshot distribution. In the total emissions estimation framework, using the snapshot emission rate distribution assumes that, with a sufficiently large sample size, the native frequency of emission events across equipment types and facility classes is well represented.

The preprocessing workflow begins by filtering job-wise data into a snapshot, defined as the first pass over an emission location, averaged over a 3-hour time window. This window allows for repeat emission rate measurements of the same source location to be averaged within a short duration to improve quantification accuracy. Typically, multiple passes over the same emission location occur within minutes due to overlapping scan swaths corresponding to adjacent flyover passes.

Next, emission locations where gas was detected but no emission rate was calculated are addressed. These cases are handled using a tiered approach. First, if a subsequent pass over of the emission location provides a flux estimate, it is used to backfill the missing value. If this is not possible, the next option is to estimate the flux based on the integrated plume concentration (IPC), a method similar to the integrated mass enhancement method 2 , which integrates the methane enhancement over the plume and converts that mass to a flux using an effective transport speed U_{eff} . In our implementation, the methane concentration is integrated across the spatial extent of the plume (IPC) and the effective transport speed (U_{eff}) is obtained by scaling the 10 m wind to the estimated plume height (from parallax) assuming a log-wind profile 3 . We determine the relationship between these variables and the source emission rate by an ordinal least squares fit of a power law function to a set of controlled release data to determine the best fit coefficients. The resulting function is,

$$Q = \left(\frac{IPC * U_{eff}}{a}\right)^b, a = 1.0456 \times 10^4, b = 0.7582$$
 (S3)

If the plume is not well formed or resolved and no flux estimate is produced by standard processing, this IPC approach provides the assigned rate, which we then bound using the observed distribution of emission rates for the same equipment type in other measured emissions.

Once the snapshot source-level emissions are prepared, the snapshot facility-level emission rate distribution is generated by aggregating (summing) the source-level emissions

within the facility polygon. This step produces a facility-level emission distribution that includes facilities with zero emissions. Finally, the facility-level snapshot emission rate distribution is stratified by facility type and serves as the inputs to the Monte Carlo simulation.

S2.2 Measured emissions component

818

819

820

821

822

823

824

825

826 827

828

829

830

831

832

833

834

835

836

837 838 This section formalizes the measured emissions component. For a plain-language description, see Section 2.3.2 of the main text. Algorithm 1 provides the pseudocode. For each facility stratum h with population size N_h , we generate B realizations by sampling N_h facilities with replacement weighted by the equipment-count CDF. For each sampled facility f and each measured source, the estimated emission rate E_{est} is bias-corrected by drawing one relative error ratio (RER) from the quantification error CDF produced from the signal-to-noise ratio (SNR) of the detected plume and wind speed at the plume location to get E_{act} . We use the convention $E_{act} = E_{est} \times RER$, where $RER = \frac{actual\ emission\ rate}{estimated\ emission\ rate}$. After bias correction we exclude sources below the threshold of 0.4 kg/h. Facility-level totals are summed to stratum totals $T_h^{(b)}$ for each realization (b = 1...B) and stored in StratumTotal[b]. The per-stratum total estimate is computed as the average of the stratum totals for each realization, $\widehat{T}_h = mean(StratumTotal)$. Basin totals are then obtained by summing \widehat{T}_h over strata.

```
Algorithm 1. Measured Emissions Component
    FOR each stratum h DO
    Initialize StratumTotal[1...B] = 0
3
       FOR realization b=1...B DO
          Sample N<sub>s</sub> facilities with replacement
          (weighted by equipment-count CDF)
          Set StratumDrawSum = 0
6
          FOR each sampled facility f DO
7
              Set FacilityTotal = 0
8
              FOR each measured source at f DO
                 Draw RER ~ RER(SNR) from distribution
9
10
                 Compute bias-corrected emission E_{act} = E_{est} x RER
11
                 IF E_{act} \ge 0.4 kg/h THEN add E_{act} to FacilityTotal
              END FOR (sources)
12
13
              Add FacilityTotal to StratumDrawSum
          END FOR (facilities)
14
          Set T_h^{(b)} = StratumDrawSum; StratumTotal[b] = T_h^{(b)}
15
16
       END FOR (realizations)
17
       Set per-stratum estimate \widehat{T_h} = mean(StratumTotal)
    END FOR (stratum)
18
```

S2.3 Missed emissions component

We modeled missed emissions at the source level within each facility stratum because the GML probability of detection (PoD) model is source-based. In each Monte Carlo realization b, we first take the bias-corrected measured source rates (algorithm 1) and partition the distribution into a full detection region (FDR; >3 kg/h; blue in Figure S3A) and a partial-detection region (PDR; 0.4-3 kg/h; red in Figure S3A). Because the bias-correction draws perturb source rates, the PDR set changes across realizations. For each PDR source j, we draw wind speed u_j and gas-concentration noise gcn_j from the distributions measured during the campaign and compute the source detection probability.

$$p_j = PoD(E_{act,j}, u_j, gcn_j)$$
 (S4)

To ensure numerical stability and realistic missed counts, we clamp $p_j \in [0.25,0.99]$. The 0.99 cap avoids divisions by small p_j in equation S6, while 0.25 reflects simulation-based lower performance bounds and aligns with detectability near the inventory's minimum threshold of 0.4 kg/h.

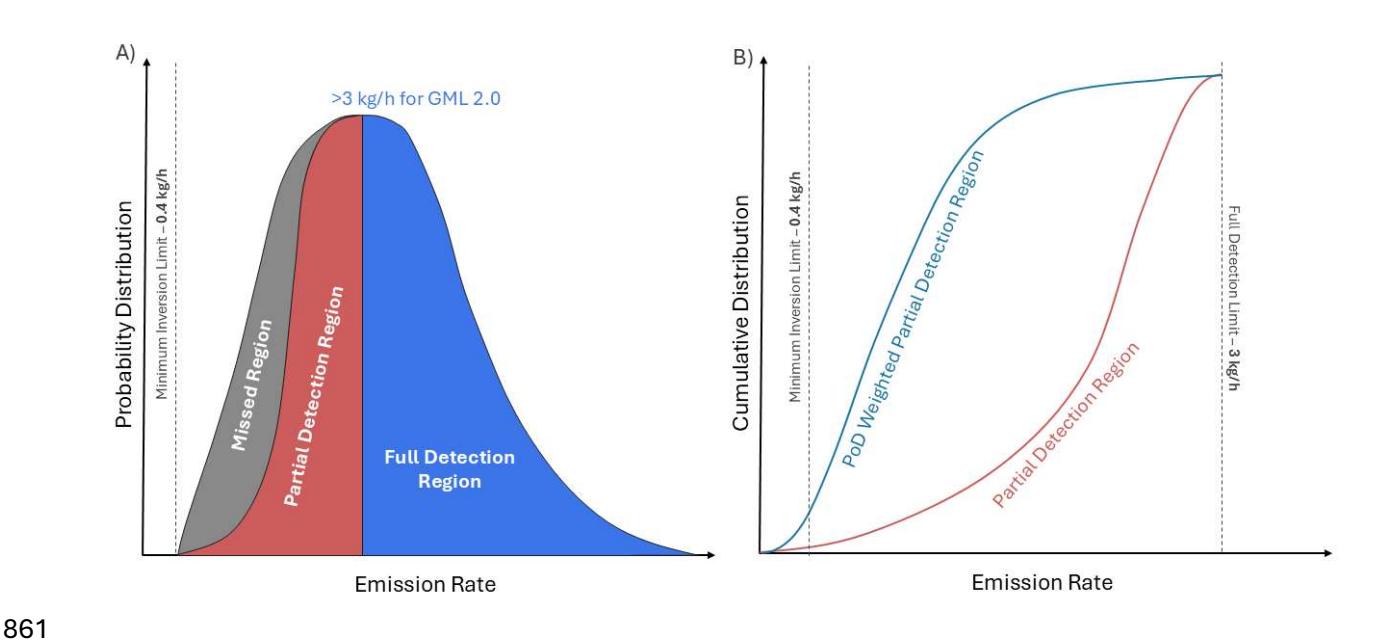
The number of missed sources $N_{miss}^{(b)}$ is then estimated using the ratio of the probability of missing a source to the probability of detecting it. In other words, this ratio represents how many missed sources are expected for each detected source, based on its probability of being detected. These ratios are summed across all sources in the PDR to obtain the estimated missed source count. Let $n^{(b)}$ be the number of PDR sources in stratum h for realization b.

$$N_{miss}^{(b)} = round\left(\sum_{j=1}^{n^{(b)}} \frac{1 - p_j}{p_j}\right)$$
 (S5)

To draw emission rates for these missed sources, we construct a PoD-weighted empirical CDF over the PDR by weighting each observed source by $w_i = (1 - p_i)$:

$$F_{miss}(e) = \frac{\sum_{j=1}^{n^{(b)}} w_j 1\{E_{act,j} \le e\}}{\sum_{j=1}^{n^{(b)}} w_j}$$
(S6)

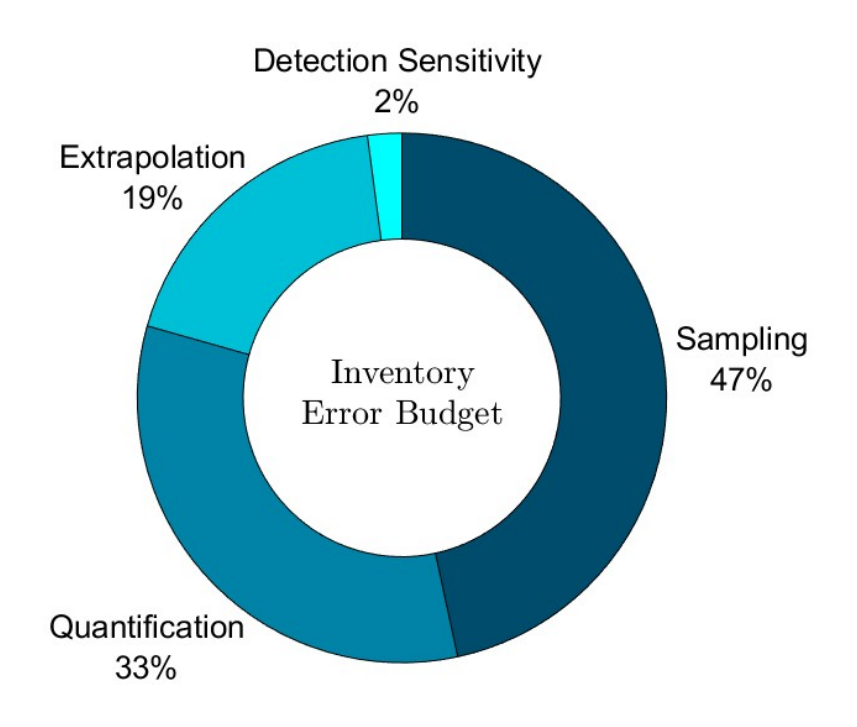
We then sample $V_j \sim Unif(0,1)$ for $j=1\dots N_{miss}^{(b)}$ and set $E_{miss,j}=F_{miss}^{-1}(V_j)$. Figure S3B illustrates the PDR CDF (red line) and the PoD weighted CDF (blue line). Finally, we add these missed draws to get the total missed emissions for the stratum realization. Uncertainty from detection probability, environmental variability, quantification error, are propagated naturally across realizations by reconstructing the PDR, recomputing p_j , and resampling F_{miss} each time.



Supplementary Figure 2. Illustration of the missed emissions estimation method. (A) Emission rate distribution segmented into three regions based on the GML probability of detection model: full detection region, partial detection region, and missed regions. (B) Example cumulative distribution of measured emissions in the partial detection region (red) and the PoD-weighted CDF used to draw emissions for the missed emissions estimate.

S2.4 Error sources

The 95% confidence interval of the total emissions estimate accounts for four main sources of error: (1) extrapolation error, (2) sampling error, (3) quantification error, and (4) detection sensitivity error. Each is quantified at the facility strata level, and when aggregating across all strata, the errors are combined in quadrature to produce the final inventory confidence interval. The error budget for the Permian inventory is shown in Figure S4



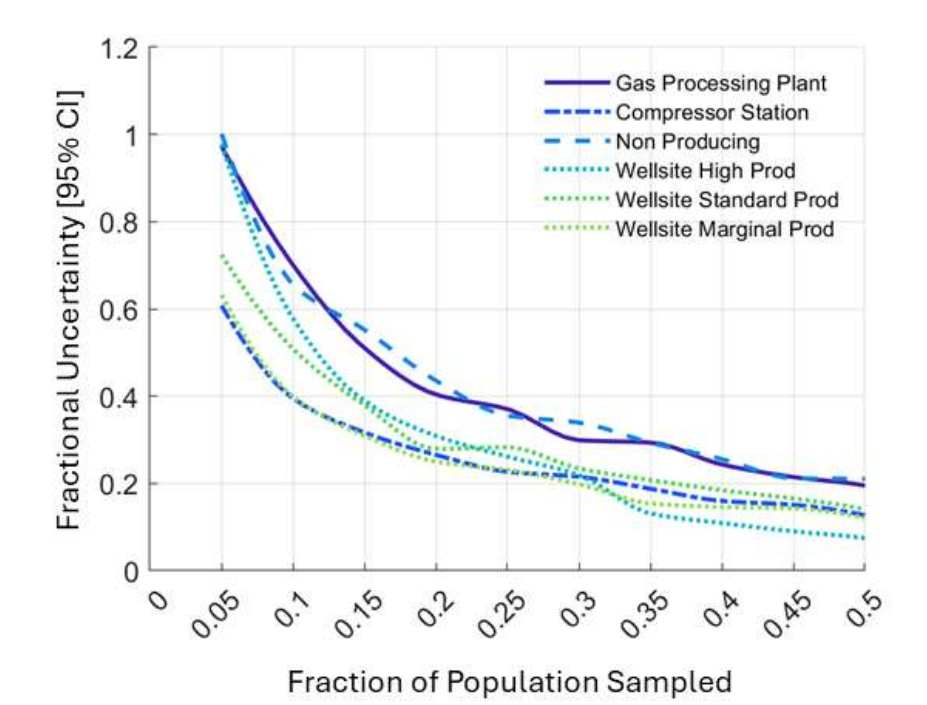
Supplementary Figure 3. Inventory error budget. Sampling 47%, Quantification 33%, Extrapolation 19%, and Detection Sensitivity 2%. Values show each component's share of total uncertainty. Percentages are rounded.

S2.4.1 Extrapolation error

Previous work using simulated emissions shows that extrapolating from right skewed emission rate distributions, such as those observed in the Permian Basin, can lead to underestimation.⁴ This occurs because the fat tail, which can significantly influence total emissions, is often poorly defined when sample sizes are limited.

To quantify extrapolation error in our emissions model, we conducted a sub-sampling experiment utilizing the large number of sources detected during this campaign. A Monte Carlo framework was implemented where, in each iteration, a random sub-sample from the full campaign dataset was drawn and then extrapolated to the total source population using draws from the distribution with replacement. This procedure was repeated for sub-sample sizes ranging from 10% to 100% of the dataset. The results (Figure S5) show how the one-sided 95% confidence interval uncertainty decreases as the sample-to-population ratio increases.

We applied this relationship to estimate extrapolation uncertainty for each facility stratum. Because our confidence intervals were derived from the complete, skewed emission distribution, this method produces conservative estimates for facility strata with lower skewness, such as marginal wellsites, and reasonable estimates for highly skewed strata, such as gas processing plants.



Supplementary Figure 4. One-sided 95% confidence interval uncertainty in total stratum emissions estimates as a function of the sampled population fraction, derived from the sub-sampling experiment.

S2.4.2 Sample error

Sampling errors are derived from Monte Carlo realizations of total extrapolated emissions. The simulation generates B potential total emission estimates, and the 95% confidence interval is defined by the 2.5 and 97.5 percentiles of these estimates. Letting the totals $T^{(1)}$... $T^{(B)}$ sorted as $T_{(1)} \le \cdots \le T_{(B)}$,

$$CI_{95\%} = [T_{([0.025B])}, T_{([0.975B])}].$$
 (S7)

Sampling error typically represents the largest source of uncertainty due to the wide range and right-skewness of emission rate distributions, causing asymmetric confidence intervals. This asymmetry emerges because some Monte Carlo realizations randomly capture large emission sources, while others do not.

S2.4.3 Quantification error

Quantification error is based on the GML quantification error model described in detail in Dudiak et al.⁵ and briefly summarized here. The model relies on controlled release tests evaluating the accuracy of GML emission estimates across varying conditions, providing both average bias corrections and uncertainty bounds for each measured emission rate. The model inputs are the local wind speed and the average gas concentration signal-to-noise ratio (SNR), a measured parameter capturing the average SNR of the methane concentration enhancement for each detected plume. The output is a relative error ratio (RER) distribution, defined as the

actual emission rate divided by the estimated emission rate. Generally, the model shows smaller emissions are typically overestimated with greater uncertainty, while larger emissions show negligible bias and smaller uncertainty. Local wind speed has minimal effect on bias but does influence uncertainty, with lower wind speeds producing greater uncertainty.

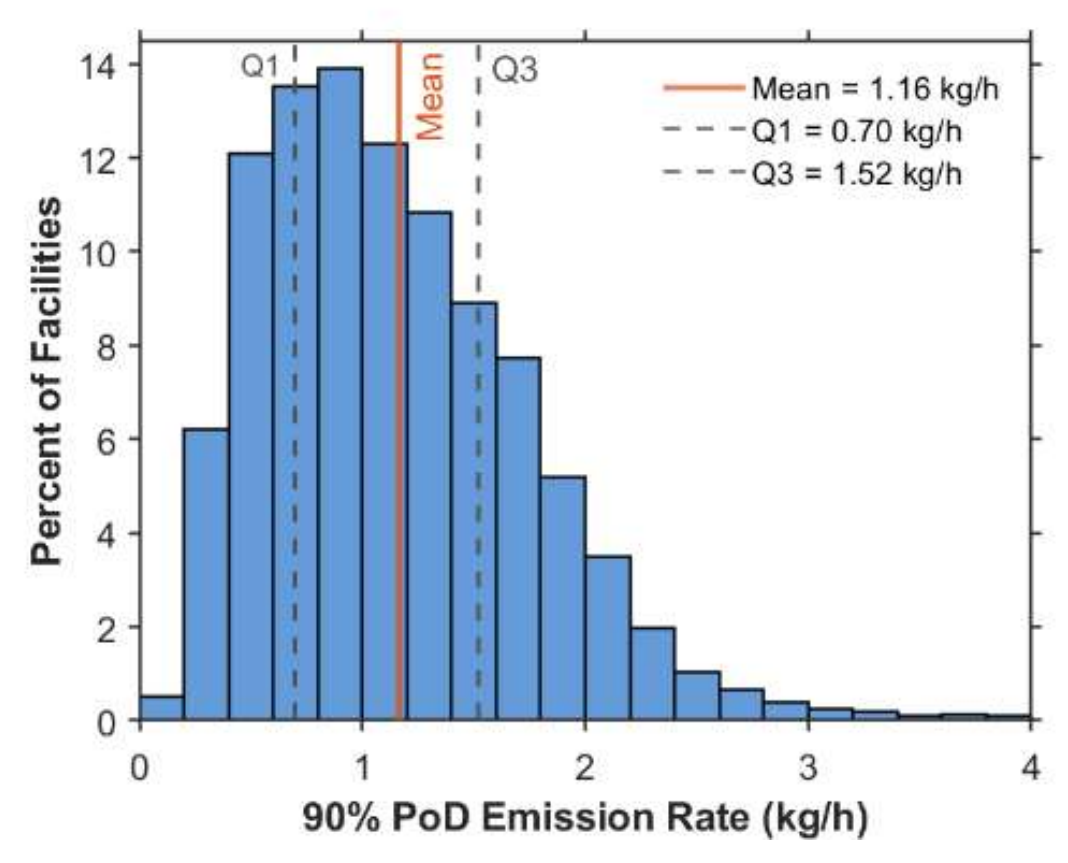
The quantification error model serves two purposes within the Monte Carlo emissions framework. First, it corrects average bias at the source level emission rates. Second, it quantifies the uncertainty bounds related to quantification error and propagates the uncertainty associated with each source to the aggregate total emissions estimate. During each simulation iteration, the cumulative distribution function of the relative error ratio (RER) is used to randomly draw an actual emission rate relative to the estimated emission rate. This process corresponds to the Quantification Bias step in the Figure 2 workflow. The adjusted emission rate is stored for each realization, and the difference between estimated and actual rates is recorded separately. The summation of these differences quantifies the bias removed from the overall estimate. After many iterations, the average source level emission rate reflects the biascorrected value. For this campaign, quantification error accounted for 33% of the total error budget.

S2.4.4 Detection sensitivity error

Detection sensitivity error represents the uncertainty associated with the missed emissions component of the total emissions estimate. As described in Section S2.3, each Monte Carlo realization includes a different number of missed emissions and draws from the partial detection distribution, resulting in variation in the total missed emissions. This error is treated similarly to sampling error for the measured emissions component (Section S2.4.2), with the 2.5 and 97.5 percentiles of the realizations used to define the 95% confidence interval. Detection sensitivity error contributed 2% to the total error budget. This contribution is relatively small because missed emissions represent a small portion of the total emissions estimate.

S3. Detection sensitivity achieved during the campaign

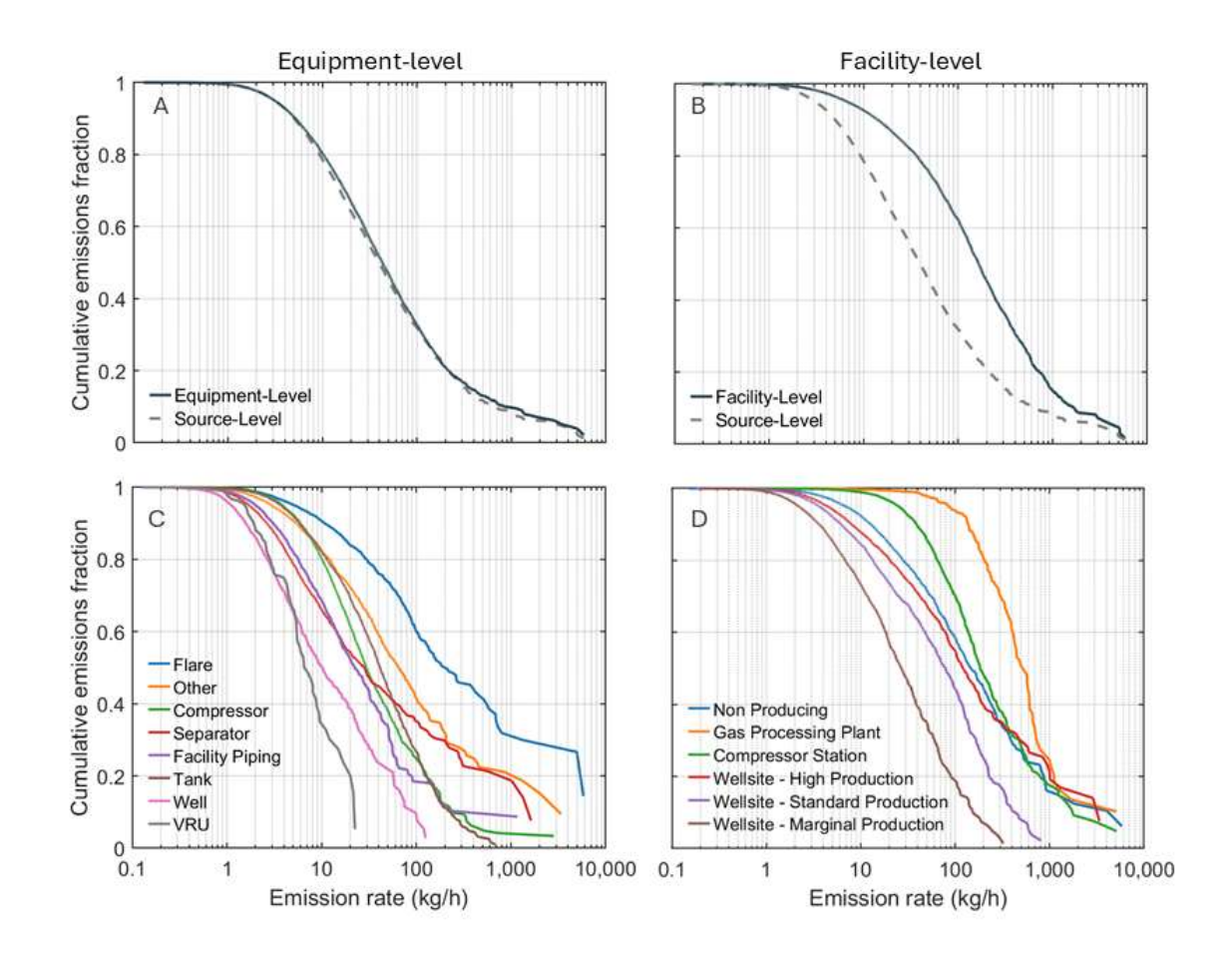
The 90% probability of detection (PoD) is the emission rate at which GML detects 90% of sources under the measured conditions of a scan. For each flyover pass on each site, we compute a PoD using the model parameterized by the wind speed and gas concentration noise recorded at the time of overflight, producing an auditable, site-specific detection sensitivity⁶. Figure S6 summarizes the achieved sensitivities across 51,770 scanned sites. The distribution centers near 1 kg/h with a mean of 1.16 kg/h and an interquartile range of 0.70–1.52 kg/h. The right tail reflects site scans made with less favorable conditions.



Supplementary Figure 5. Distribution of emission rates correspond to the 90% probability of detection (PoD) for all sites scanned during the campaign. The mean is 1.16 kg/h (red line) and the interquartile range spans 0.70 kg/h (Q1) to 1.52 kg/h (Q3).

S4. Measured emissions distributions

The cumulative share of methane emissions as a function of emission rate for equipment- and facility-level aggregation are shown in Figure S7 A) and B), respectively. The gray dashed line in these figures represents the cumulative share of emissions disaggregated at the source-level. Since detection sensitivity is a property of individual methane plumes, and most plumes correspond to a single source location, the source-level distribution can be used to estimate the fraction of emissions that would be detectable by a technology if it had a step function detection sensitivity limit at the emission rate shown on the x-axis. For example, a sensor with a step function detection limit of 10 kg/h, 20 kg/h, and 100 kg/h would detect 78%, 63%, and 31% of the emissions detected by GML, respectively. The cumulative emissions distributions by equipment and facility stratum are shown in Figure S7 C) and D), respectively.



Supplementary Figure 6. Cumulative share of methane emissions as a function of emission rate (kg/h; log scale). (A) Equipment-level and (B) facility-level distributions, where individual source emissions are summed to the corresponding piece of equipment or facility. The gray dashed line shows the underlying source-level distribution, and because detection sensitivity is a property of individual plumes, it indicates the fraction detectable by a step-function detection limit at the x-axis value. (C) Equipment-level distributions by equipment category, and (D) facility-level distributions by facility stratum.

S5. Measurement-based emissions factors

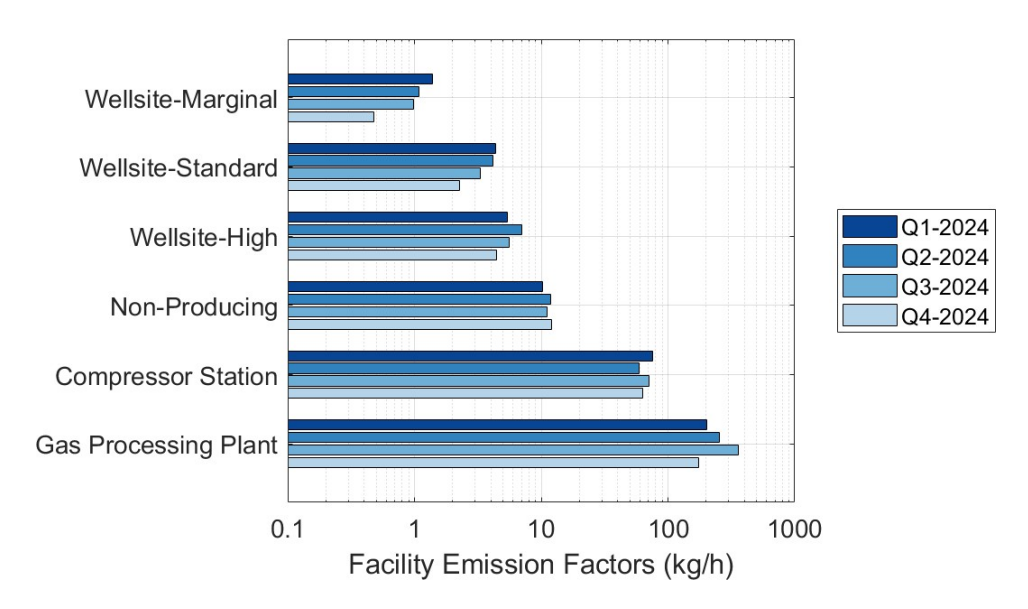
We report emission factors as total methane emissions from a stratum divided by the total number of entities in that stratum, counting non-emitting entities as zero. Totals are derived from our stratified Monte Carlo workflow applied to the 2024 campaign; counts include all scanned entities.

$$Facility \ EF_g = \frac{Total \ emissions \ from \ facilities \ in \ stratum \ g}{Total \ number \ of \ facilities \ in \ stratum \ g} = \frac{E_g^{total}}{N_g} \tag{S8}$$

Equipment
$$EF_k = \frac{Total\ emissions\ from\ equipment\ type\ k}{Total\ number\ of\ units\ of\ equipment\ type\ k} = \frac{E_k^{total}}{U_k}$$
 (S9)

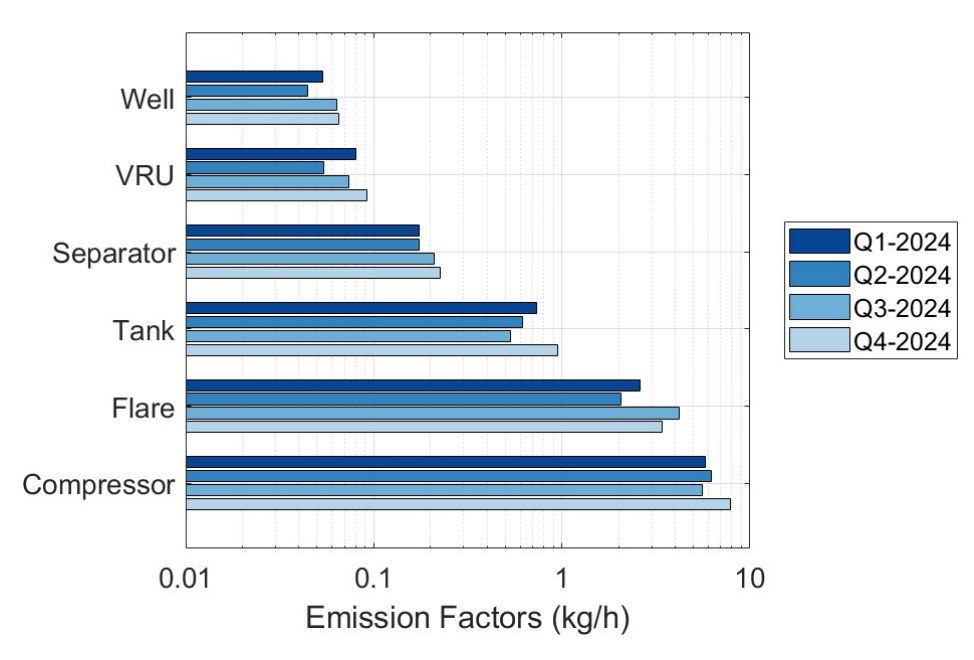
Here $E_g^{\rm total}$ and $E_k^{\rm total}$ are the Monte Carlo derived totals for the analysis period, and N_g and U_k are the complete facility and unit counts, respectively, including entities with no detected emissions.

S5.1 Facility-level



Supplementary Figure 7. Facility emission factors by stratum for each quarter of 2024. Horizontal bars show the estimated emission factor (kg/h per facility) for Q1–Q4 on a logarithmic x-axis.

S5.2 Equipment-level



Supplementary Figure 8. Equipment emission factors for each quarter of 2024. Horizontal bars show the estimated emission factor (kg/h per equipment unit) for Q1–Q4 on a logarithmic x-axis.

S6. Previously published inventories

Supplementary Table 4. Published estimates of methane loss rate for the Permian Basin presented in Figure 8 of the main text. Loss rate is the percentage of methane emitted relative to produced gas Bracketed values report the study's uncertainty interval provided. Where needed, loss rates were harmonized to a methane fraction of 0.90 for comparability. Barkley et al. represent the Delaware subbasin and no methane fraction was reported. All other studies cover the broader Permian.

Study	Measurement	Region	Measurement	Loss Rate (%)
	Year	Region	Method	LUSS Nate (70)
Shen et al. 2022 ⁷	2019	Permian	Satellite	3.20 [2.49, 4.00]
Varon et al. 2023 ⁸	2019	Permian	Satellite	4.00 [3.02, 4.98]
Sherwin et al. 2024 ⁹	2019	Permian	Aerial	5.29 [5.08, 5.53]
Barkley et al. 2024 ¹⁰	2020-2022	Permian -	Ground-based	3.00 [2.50-3.50]
Dai kiey et al. 2024	2020-2022	Delaware	tower network	3.00 [2.30-3.30]
Omara et al. 2024 ¹¹	2021	Permian	Ground-based	2.58 [2.13, 3.38]
Varon et al. 2025 ¹²	2023	Permian	Satellite	2.84 [2.04, 3.64]
This Study	2024	Permian	Aerial	3.13 [2.47, 3.85]

S7. Methane emission intensity calculation

Several production-normalized emission metrics are used to indicate performance, but no standard currently exists. The terms *loss rate* and *intensity* are sometimes used interchangeably, though they may refer to different calculations. To facilitate comparisons between studies, it is important to understand which metric is being applied. In this analysis, intensity was calculated using three methods.

The first, referred to here as methane loss rate, is defined as emitted methane divided by methane produced in natural gas, expressed as a percentage. This metric tends to favor gasdominant basins such as Marcellus and disadvantage oil-rich basins like the Permian, as it considers only gas production in the denominator.

$$Methane\ Loss\ Rate\ (\%) = \frac{Methane\ Emissions}{Methane\ in\ Produced\ Natural\ Gas} \tag{S10}$$

The second metric, referred to as NGSI methane intensity, follows a standardized protocol developed by the Natural Gas Sustainability Initiative. This approach allocates a portion of the total methane emissions to natural gas production based on its share of total energy produced across all hydrocarbons (e.g., oil and condensate). This allocation is made on an energy basis and is represented by the gas ratio term in the equation below. This metric provides a better comparative metric across different types of oil and gas basins relative to the methane loss rate.

$$NGSI Methane Intensity (\%) = \frac{Methane Emissions * Gas Ratio}{Methane in Produced Natural Gas}$$
(S11)

The third metric, the methane emission factor¹³, is the mass of emitted methane per marketed energy. Normalizing by energy output enables straightforward comparisons across basins, though it is reported in g CH₄ MJ⁻¹ rather than a percentage, which is generally easier to interpret.

Methane Emission Factor
$$\left(\frac{g}{MJ}\right) = \frac{Methane\ Emissions}{Produced\ Energy}$$
 (S12)

Assumptions regarding the methane content of produced natural gas and energy conversion factors are required to calculate methane intensity. Natural gas composition can vary widely, with methane content typically ranging from 70% to 98% by volume. For this analysis, we assume a conservative methane fraction of 90% for natural gas produced in the Permian Basin, consistent with assumptions made in the recent inventory developed by ⁹. Note that if the actual methane fraction is lower than this assumption, the resulting methane intensity would be higher. The following conversion factors are used to convert oil and gas production volumes to an energy basis:

- Methane Density: 0.0192 metric tons per Mscf ¹⁴
- Natural Gas: 1.02 MMBtu per Mscf ¹⁵
- Crude Oil: 5.8 MMBtu per barrel 15

S8. References

1014

1015 1016

1017

1018

1019

1020 1021

1022

1025

- 1026 (1) Neyman, J. On the Two Different Aspects of the Representative Method: The Method of Stratified Sampling and the Method of Purposive Selection. *Journal of the Royal Statistical Society* **1934**, *97* (4), 558–625. https://doi.org/10.2307/2342192.
- (2) Varon, D. J.; Jacob, D. J.; McKeever, J.; Jervis, D.; Durak, B. O. A.; Xia, Y.; Huang, Y.
 Quantifying Methane Point Sources from Fine-Scale Satellite Observations of Atmospheric
 Methane Plumes. *Atmos. Meas. Tech.* 2018, 11 (10), 5673–5686.
 https://doi.org/10.5194/amt-11-5673-2018.
- 1033 (3) Thorpe, M. J.; Kreitinger, A.; Altamura, D. T.; Dudiak, C. D.; Conrad, B. M.; Tyner, D. R.;
 1034 Johnson, M. R.; Brasseur, J. K.; Roos, P. A.; Kunkel, W. M. Deployment-Invariant Probability
 1035 of Detection Characterization for Aerial LiDAR Methane Detection. *Remote Sensing of*1036 *Environment* 2024, 315, 114435.
- 1037 (4) Schissel, C.; Allen, D.; Dieter, H. Methods for Spatial Extrapolation of Methane
 1038 Measurements in Constructing Regional Estimates from Sample Populations. *Environ. Sci.*1039 *Technol.* **2024**, *58* (6), 2739–2749. https://doi.org/10.1021/acs.est.3c08185.
- 1040 (5) Dudiak, C. D.; Goodwin, D. B.; Altamura, D. T.; Donahue, C. P.; Thorpe, M. J. Quantification 1041 Error Model for Aerial LiDAR Methane Emission Rate Estimates. *Manuscript In Preparation* 1042 **2025**.

- 1043 (6) Thorpe, M. J. Deployment-Invariant Probability of Detection Characterization for Aerial
 1044 LiDAR Methane Detection. *Remote Sensing of Environment* 2024, 315, 114435.
 1045 https://doi.org/10.1016/j.rse.2024.114435.
- 1046 (7) Shen, L.; Gautam, R.; Omara, M.; Zavala-Araiza, D.; Maasakkers, J. D.; Scarpelli, T. R.;
 1047 Lorente, A.; Lyon, D.; Sheng, J.; Varon, D. J.; Nesser, H.; Qu, Z.; Lu, X.; Sulprizio, M. P.;
 1048 Hamburg, S. P.; Jacob, D. J. Satellite Quantification of Oil and Natural Gas Methane
 1049 Emissions in the US and Canada Including Contributions from Individual Basins. *Atmos.*1050 *Chem. Phys.* 2022, *22* (17), 11203–11215. https://doi.org/10.5194/acp-22-11203-2022.
- Varon, D. J.; Jacob, D. J.; Hmiel, B.; Gautam, R.; Lyon, D. R.; Omara, M.; Sulprizio, M.; Shen, L.; Pendergrass, D.; Nesser, H.; Qu, Z.; Barkley, Z. R.; Miles, N. L.; Richardson, S. J.; Davis, K. J.; Pandey, S.; Lu, X.; Lorente, A.; Borsdorff, T.; Maasakkers, J. D.; Aben, I. Continuous Weekly Monitoring of Methane Emissions from the Permian Basin by Inversion of TROPOMI Satellite Observations. *Atmos. Chem. Phys.* 2023, 23 (13), 7503–7520. https://doi.org/10.5194/acp-23-7503-2023.
- (9) Sherwin, E. D.; Rutherford, J. S.; Zhang, Z.; Chen, Y.; Wetherley, E. B.; Yakovlev, P. V.;
 Berman, E. S. F.; Jones, B. B.; Cusworth, D. H.; Thorpe, A. K.; Ayasse, A. K.; Duren, R. M.;
 Brandt, A. R. US Oil and Gas System Emissions from Nearly One Million Aerial Site
 Measurements. *Nature* 2024, 627 (8003), 328–334. https://doi.org/10.1038/s41586-024-07117-5.
- (10) Barkley, Z.; Davis, K.; Miles, N.; Richardson, S.; Deng, A.; Hmiel, B.; Lyon, D.; Lauvaux, T.
 Quantification of Oil and Gas Methane Emissions in the Delaware and Marcellus Basins
 Using a Network of Continuous Tower-Based Measurements. *Atmos. Chem. Phys.* 2023, 23
 (11), 6127–6144. https://doi.org/10.5194/acp-23-6127-2023.
- (11) Omara, M.; Himmelberger, A.; MacKay, K.; Williams, J. P.; Benmergui, J.; Sargent, M.; Wofsy,
 S. C.; Gautam, R. Constructing a Measurement-Based Spatially Explicit Inventory of US Oil
 and Gas Methane Emissions (2021). *Earth Syst. Sci. Data* 2024, *16* (9), 3973–3991.
 https://doi.org/10.5194/essd-16-3973-2024.
- (12) Varon, D. J.; Jacob, D. J.; Estrada, L. A.; Balasus, N.; East, J.; Pendergrass, D. C.; Chen, Z.;
 Sulprizio, M. P.; Omara, M.; Gautam, R. Seasonality and Declining Intensity of Methane
 Emissions from the Permian and Nearby US Oil and Gas Basins. 2025.
- 1073 (13) Johnson, M. R.; Conrad, B. M.; Zimmerle, D. J.; Kleinberg, R. L. Methane by the Numbers: 1074 The Need for Clear and Comparable Methane Intensity Metrics. EarthArXiv 2025.
- (14) Natural Gas Sustainability Initiative. NGSI Methane Emissions Intensity Protocol Version
 1.0, 2021. https://www.aga.org/wp content/uploads/2022/12/ngsi_methaneintensityprotocol_v1.0_feb2021.pdf (accessed
 2025-07-02).
- 1079 (15) GTI Energy. Veritas Methane Emissions Intensity Protocol Version 2, 2023.

1080